

AIX-MARSEILLE UNIVERSITY  
DOCTORAL SCHOOL: Physics and Material Science  
PARTENAIRES DE RECHERCHE  
Laboratoire MADIREL

Submitted with the view of obtaining the degree of doctor

Discipline: Material Science  
Specialty: Characterisation of porous materials

Paul A. Iacomi

Titre de la thèse: sous-titre de la thèse

Defended on JJ/MM/AAAA in front of the following jury:

Prénom NOM	Affiliation	Rapporteur
Prénom NOM	Affiliation	Rapporteur
Prénom NOM	Affiliation	Examinateur
Prénom NOM	Affiliation	Examinateur
Prénom NOM	Affiliation	Examinateur
Prénom NOM	Affiliation	Directeur de thèse

National thesis number: 2017AIXM0001/001ED62



This work falls under the conditions of the [Creative Commons Attribution License - No commercial use - No modification 4.0 International](#).

# Abstract

Abstract is here.

# Acknowledgements

Acknowledgements go here

# Contents

<b>Abstract</b>	iii
<b>Acknowledgements</b>	iv
<b>1. Building a framework for adsorption data processing</b>	1
1.1. Introduction . . . . .	1
1.2. pyGAPS overview . . . . .	1
1.2.1. Intended use cases . . . . .	1
1.2.2. Core structure . . . . .	2
1.2.3. Creation of an Isotherm . . . . .	3
1.2.4. Workflow . . . . .	3
1.2.5. Units . . . . .	5
1.3. Isotherm characterisation and fitting . . . . .	5
1.3.1. Mathematical descriptions of isotherms . . . . .	5
1.3.2. Specific surface area and pore volume calculations . . . . .	13
1.3.3. Assessing porosity . . . . .	19
1.3.4. Predicting multicomponent adsorption . . . . .	27
1.4. Case studies . . . . .	29
1.5. Conclusion . . . . .	29
<b>2. Extending bulk analysis of porous compounds through calorimetry</b>	34
2.1. Introduction . . . . .	34
2.2. Literature . . . . .	34
2.3. Method . . . . .	34
2.4. Results and discussion . . . . .	35
2.4.1. Routine characterization of a MOF sample . . . . .	35
2.4.2. Analysis of a carbon sample for gas separation applications . . . . .	37
2.5. Conclusion . . . . .	37
<b>3. Exploring the impact of synthesis and defects on adsorption measurements</b>	40
3.1. Introduction . . . . .	40
3.2. Literature . . . . .	40
3.3. Method . . . . .	40
3.4. Results and discussion . . . . .	40
3.5. Conclusion . . . . .	40
<b>4. Exploring the impact of material form on adsorption measurements</b>	42
4.1. Introduction . . . . .	42
4.2. Shaping in context . . . . .	43

## *Contents*

4.3.	Synthesis, shaping and characterisation . . . . .	44
4.3.1.	Material Synthesis . . . . .	44
4.3.2.	Shaping Procedure . . . . .	45
4.3.3.	Characterisation of powders and pellets . . . . .	45
4.3.4.	Sample activation for adsorption . . . . .	45
4.4.	Results and discussion . . . . .	46
4.4.1.	Thermal stability . . . . .	46
4.4.2.	Adsorption isotherms at 77K and room temperature . . . . .	46
4.4.3.	Room temperature gas adsorption and microcalorimetry . . . . .	49
4.4.4.	Vapour adsorption . . . . .	55
4.5.	Conclusion . . . . .	57
<b>5.</b>	<b>Exploring novel behaviours</b>	<b>63</b>
5.1.	Introduction . . . . .	63
5.2.	Literature . . . . .	63
5.3.	Method . . . . .	63
5.4.	Results and discussion . . . . .	63
5.5.	Conclusion . . . . .	63
<b>A.</b>	<b>Common characterisation techniques</b>	<b>65</b>
A.1.	Thermogravimetry . . . . .	65
A.2.	Bulk density determination . . . . .	65
A.3.	Skeletal density determination . . . . .	65
A.4.	Nitrogen physisorption at 77 K . . . . .	66
A.5.	Vapour physisorption at 298 K . . . . .	66
A.6.	Gravimetric isotherms . . . . .	66
<b>B.</b>	<b>Synthesis method of referenced materials</b>	<b>68</b>
B.1.	Takeda 5A reference carbon . . . . .	68
B.2.	MCM-41 controlled pore glass . . . . .	68
B.3.	Zr fumarate MOF . . . . .	68
B.4.	UiO-66(Zr) for defect study . . . . .	68
B.5.	UiO-66(Zr) for shaping study . . . . .	69
B.6.	MIL-100(Fe) for shaping study . . . . .	69
B.7.	MIL-127(Fe) for shaping study . . . . .	69
<b>C.</b>	<b>Complete adsorption dataset for shaping study</b>	<b>71</b>
C.1.	Calorimetry dataset UiO-66(Zr) . . . . .	71
C.2.	Calorimetry MIL-100(Fe) . . . . .	72
C.3.	Calorimetry MIL-127(Fe) . . . . .	75

# 4. Exploring the impact of material form on adsorption measurements

## 4.1. Introduction

An adsorbent cannot be used in an industrial process in its raw powder form. The small crystals which are normally the synthesis product of such a material would not be suited for direct use. Therefore, in order to use an adsorbent in a setting such as the beds and columns common in catalysis, PSA (pressure swing adsorption) and TSA (temperature swing adsorption), a structuring into a hierarchically porous structure form is needed <sup>(1)</sup>.

To this end adsorbents are usually shaped into pellets, a process which introduces a range of benefits, such as improved flow regimes, better thermal management and material containment. The shaping process is needed not just for stabilising the small particles, but also to impart the resulting pellet with a high enough mechanical resistance to withstand the stresses imposed by the high flow encountered in an industrial bed.

The shaping process is therefore a crucial step towards the large-scale use of an adsorbent material. Even for commonplace adsorbents such as carbons and zeolites, the optimum binding compound and the shaping process itself are the subject of extensive research. Often, the procedure is tailored for individual material and application. In an ideal setting, the process has limited effects on the properties of the material. However, this is often not the case, as shaping can change adsorption performance dramatically.

As metal organic frameworks with properties that make them suited for industrial applications emerge, a push towards obtaining shaped versions of the best-performing materials is seen, first for pilot studies and perhaps large scale use.

Due to the wide range of materials, potential shaping methods, binders and effects introduced through the process itself, a high-throughput methodology is often the kind of approach that is best suited to exhaustively explore the result space. The data processing methodologies discussed in [chapter 1](#) combined with thermal methods presented in [chapter 2](#) are put to use in a study on the shaping performance of MOFs.

After a short introduction to shaping, this chapter explores the variability introduced by an  $\rho$ -alumina binder in three topical MOFs: UiO-66(Zr), MIL-100(Fe) and MIL-127(Fe). These MOFs have been selected for their known chemical and thermal stability and well-studied adsorption behaviour. The alumina shaped variant of these MOFs is compared to the original powder material with regard to the adsorption of a series of common gasses and vapours. Microcalorimetry in conjunction with 8 gas probes has been used to get an in-depth picture of the change in surface energetics. Finally, a previous study on the same materials shaped with a poly-vinyl alcohol (PVA) binder is extended to vapour adsorption and the entire dataset is processed to obtain an overview of the impact of a hydrophobic and a hydrophilic binder on adsorption performance.

## 4.2. Shaping in context

The kinetics of the adsorption process are generally improved by the multi-scale pore size distribution afforded through shaping. Capacity per mass of pellet is expected to decrease due to the addition of a non-porous component, but the difference should be small and should not arise due to effects such as pore blocking or pore filling with the binder material. Furthermore, the densification effect is expected to lead to better performance on a volume basis. Finally, binder addition should not influence the chemical properties of the adsorbent, and preserve the original interactions with the adsorbate. With a judicious choice of binding material, the resulting pellet should outperform the powder.

For carbons, binders such as pitch, polymers (CMC, PVA) or even non-porous carbon black are commonly used.<sup>(2)</sup> Often, a combination of binders is used, each with a different task during the pelletization process.<sup>(3)</sup> The process itself consists of extrusion of the particle-binder slurry and then hardening either through temperature, cross-linking or chemical treatment. Other methods, such as spray-drying or granulation can similarly be used.<sup>(4)</sup>

For zeolites, inorganic binders are more prevalent, with silica, alumina and clay binders commonly used in industry. It has been shown<sup>(5,6)</sup> that the choice of binder can introduce large property variations, ranging from loss of porosity and structure to the enhancement of the desired reactivity and selectivity through changes in the acid site density or ion migration.

The shaping of MOFs has been attempted with a wide range of binders and methods. Methods such as granulation, spray-drying or extrusion have all been successfully employed to create MOF pellets.<sup>(7)</sup> Monoliths have also been shown to be an effective way for shaping purposes, either through impregnation<sup>(8)</sup> or through support on alumina.<sup>(9)</sup> Surprisingly, compression<sup>(10)</sup> or even simple air drying of MOF slurries<sup>(11)</sup> have also shown good results. Note that the ZIF-8 monolith prepared through the latter method had a three times larger volumetric specific surface area than the conventional powder.

The connection between MOF and binder is also of crucial importance for membranes. The MOF-polymer interface has been shown<sup>(12)</sup> to be subject to a complex interplay of interactions between the organic chains and the crystal surfaces. These effects can be striking enough to warrant further research into MOF-polymer hybrids,<sup>(13)</sup> with the aim of combining the unique attributes of both materials.

Previous work from this group<sup>(14)</sup> has analysed the impact of PVA shaping on a series of MOFs. It was shown that the binder did introduce some specific effects, such as a protection effect on the reduction of  $\text{Fe}^{3+}$  to  $\text{Fe}^{2+}$  in MIL-127(Fe), as well as a curious gating effect seen on butane adsorption on MIL-100(Fe), likely due to polymer chains covering pore entrances. Otherwise, the shaping imparted good performance to the shaped samples, with almost no capacity loss on a mass basis. Unfortunately, the use of a polymer limited the activation temperature of the samples to a maximum of 150 °C.

In this work we have selected the same series of “topical” MOFs and have investigated the influence of a different shaping method, namely the use of alumina binder, on their

shaping  
meth-  
ods

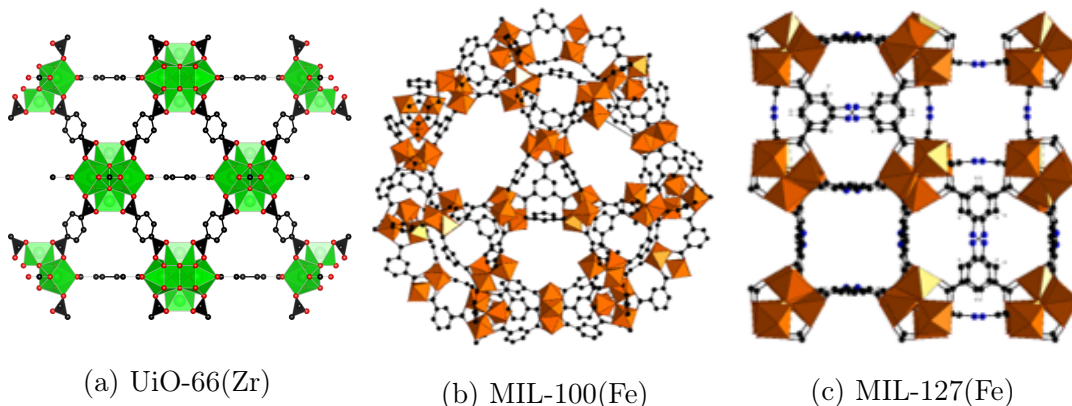


Figure 4.1.: The unit structures of the investigated MOFs. The colour coding is as follows: Zr polyhedra in green, Fe octahedra in brown, C in black, O in red, N in blue. Hydrogen atoms are omitted for clarity.

adsorption properties.

The UiO-66(Zr) MOF and its derivatives are well known due to their stability, both in regards to temperature and chemical compounds.<sup>(15)</sup> It is composed of Zr6-oxo clusters which are connected with benzene dicarboxilate (BDC) linkers to form a face-centered cubic framework. It has shown promise<sup>(16)</sup> in use for gas adsorption applications.

MIL-100(Fe) is a MOF which uses the benzene tricarboxilate (BTC) linker in conjunction with trimeric iron (III) octahedral clusters .<sup>(17)</sup> The framework assembles in hybrid supertetrahedra which leads to very large pore sizes. The iron trimers are coordinated with anions and have shown a propensity to partially reduce to a divalent  $\text{Fe}^{2+}$  state, exposing a naked metal site in the process.<sup>(18)</sup>

The last material, MIL-127(Fe), originally reported by Liu et al. is a MOF built from the same metal (III) octahedra trimers as MIL-100(Fe), but using the 3,3',5,5'-azobzenetetracarboxylate (TazBz) linker, to produce a framework with the (soc) topology. This material has shown promise<sup>(20)</sup> for large scale synthesis. Furthermore, due to its alternating hydrophobic/hydrophilic microporous systems, it has been shown to be of interest for multiple applications such as catalysis or  $\text{CO}_2$  capture.<sup>(21)</sup>

The structures of the three materials can be seen in Figure 4.1.

## 4.3. Synthesis, shaping and characterisation

### 4.3.1. Material Synthesis

The synthesis of these MOFs is well described in literature, as it has been previously reported for UiO-66(Zr)<sup>(15)</sup> and MIL-100(Fe).<sup>(22)</sup>

The UiO-66(Zr) and MIL-100(Fe) powders have been synthesised at the Korea Research Institute of Chemical Technology (KRICT) according to the methods previously referenced. Complete details of the synthesis method can be found in the related publi-

#### 4. Exploring the impact of material form on adsorption measurements

cation<sup>(23)</sup> and in Appendix B.

##### 4.3.2. Shaping Procedure

The shaping of the samples also took place at KRICT and was done using a wet granulation method. In the case of the alumina binder, the MOF powder was mixed with the previously prepared mesoporous  $\rho$ -alumina with water added as the dispersing medium. For the PVA binder, the MOF powder was instead added to a solution of ethanol solution containing a polymer mixture of polyvinyl groups such as polyvinyl alcohol and polyvinyl butyral. The resulting mixture was shaped into beads using a hand-made pan granulator. During the process, the spheres were sprayed with the respective solvent in order to achieve desired size. The beads were then sieved and rolled using a roller machine to enhance their spherical shape. Finally, the prepared samples were dried at 303K for 12 h to remove all residual solvent. The resulting beads were near spherical in shape, with a diameter between 2 mm to 2.5 mm.

##### 4.3.3. Characterisation of powders and pellets

The primary interest of the study was observing differences in adsorption properties between the powder and the shaped materials.

Thermogravimetric analysis was used to verify that the binder did not change the thermal stability of the materials and, in the case of the PVA variant, to ensure that the activation temperature chosen did not induce polymer decomposition. The TGA method is described in detail in Appendix A.1.

The bulk and skeletal density of the powder and pellets were measured to allow isotherms to be presented on a volume basis, as well as to check the level of densification afforded through the shaping process. The procedure is described in Appendix A.2 and Appendix A.3.

Specific surface area and pore volume were determined through nitrogen adsorption at 77 K. These measurements were recorded according to the method in Appendix A.4. For inspecting changes in surface hydrophobicity, water and methanol adsorption isotherms were measured according to the method presented in Appendix A.5.

Finally, all calorimetry data was recorded using the high sensitivity Tian-Calvet calorimeter coupled with adsorption volumetry, as introduced in chapter 2.

##### 4.3.4. Sample activation for adsorption

The materials were pre-treated before all adsorption experiments by activation at high temperature under secondary vacuum for 16 hours. The activation temperature was specific to each solid: 200 °C for UiO-66(Zr), 150 °C for MIL-100(Fe) and 150 °C for MIL-127(Fe).

## 4.4. Results and discussion

### 4.4.1. Thermal stability

In order to check if the shaped samples have not undergone bulk structural changes, as well as find a suitable activation temperature, the powder and shaped samples underwent thermogravimetric analysis under an argon atmosphere.

The process of shaping did not have any impact on the thermal stability of the investigated MOFs, as evidenced by the TGA curves in [Figure 4.2](#). The primary mass loss occurs in a 10 °C range for all powder-pellet pairs. Shaped samples are also seen to have a smaller mass loss at high temperatures. This is expected, as after the addition of temperature inert alumina, the MOF makes up a lower percentage of the material.

### 4.4.2. Adsorption isotherms at 77K and room temperature

Nitrogen sorption isotherms measured at 77 K have been measured on both powder and  $\rho$ -alumina pellets, with the isotherms presented in [Figure 4.3](#). Observation of the physisorption curves sheds light on the impact of the alumina binder on the materials chosen. The shapes of all isotherms are visually similar, with the pellet curves shifted downwards due to the aforementioned structure degradation. In both powders and pellets, the increased uptake after  $0.9 p/p^0$  is a sign of condensation in very large pores or voids, which can be attributed to intra-pellet spaces and crystal agglomeration. In the MIL-127(Fe) pellets, a narrow hysteresis curve is seen, which closes at a  $p/p^0$  of 0.5. This curve corresponds to capillary condensation in a pore size of around 4 nm. This pore width is too small to be a sign of inter-pellet voids and therefore must be a consequence of the shaping process.

While no other significant features are visible on the isotherms themselves, we use pyGAPS to further process them and obtain properties such as specific surface area, calculated through the BET method and pore volume, calculated as the volume of nitrogen adsorbed at a  $p/p^0$  of 0.2. As the surface area of the binder is lower than the one of the MOF, a drop in both these properties is expected. The calculated values are shown in [Table 4.1](#).

Table 4.1.: Properties of the studied powders and pellets

MOF	form	BET surface area	Pore volume	Bulk density
UiO-66(Zr)	powder	903	0.38	0.3192
	$\rho$ -alumina	619	0.24	0.4724
MIL-100(Fe)	powder	1928	0.78	0.2165
	$\rho$ -alumina	1451	0.6	0.3512
MIL-127(Fe)	powder	1400	x	0.412
	$\rho$ -alumina	1266	0.49	0.526

As predicted, the specific surface area of the shaped samples is decreased compared to

#### 4. Exploring the impact of material form on adsorption measurements

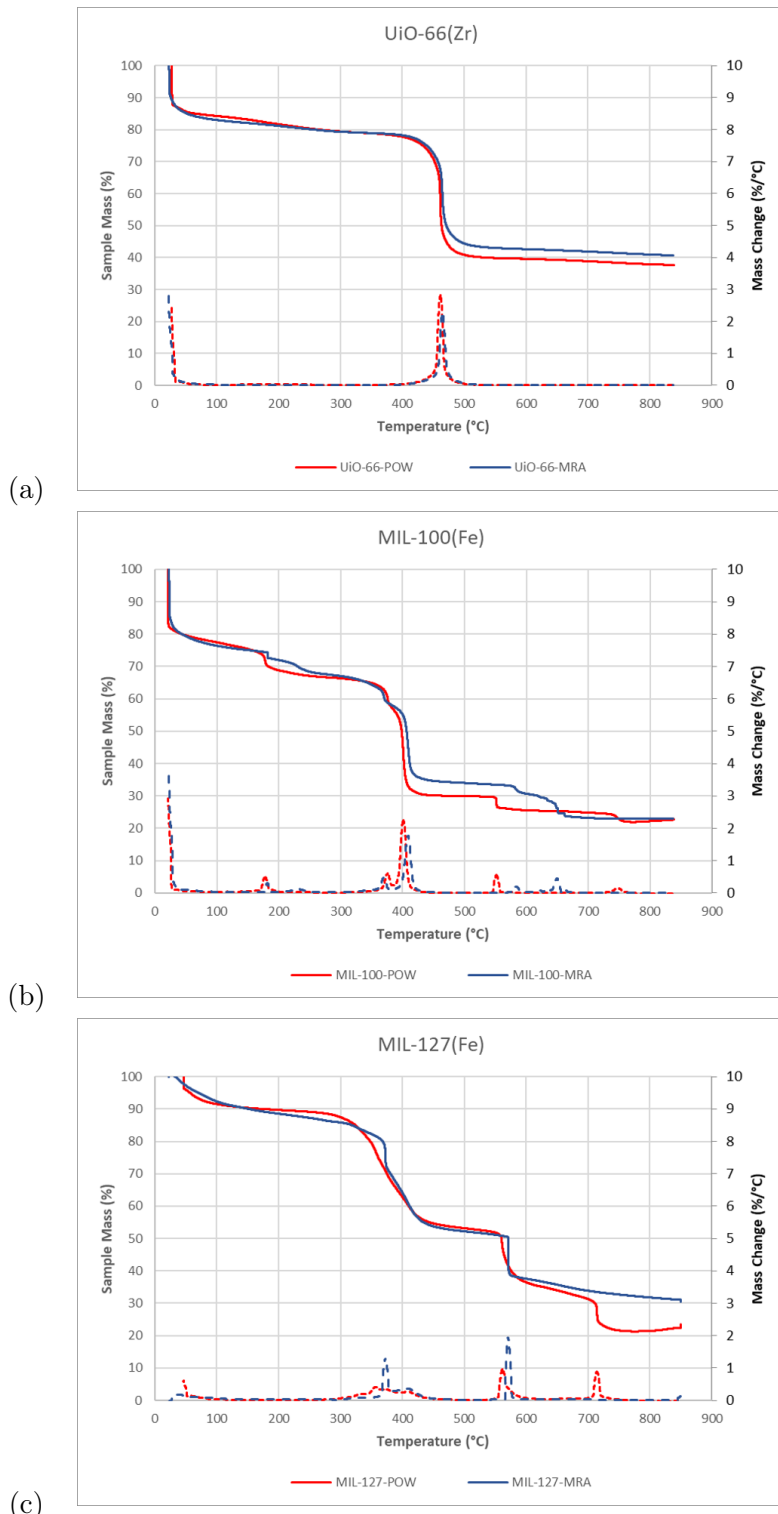


Figure 4.2.: High resolution TGA curves recorded under argon on (a)  $\text{UiO-66}(\text{Zr})$ , (b)  $\text{MIL-100}(\text{Fe})$  and (c)  $\text{MIL-127}(\text{Fe})$ . The original powders are depicted in red and the shaped material in blue.

#### 4. Exploring the impact of material form on adsorption measurements

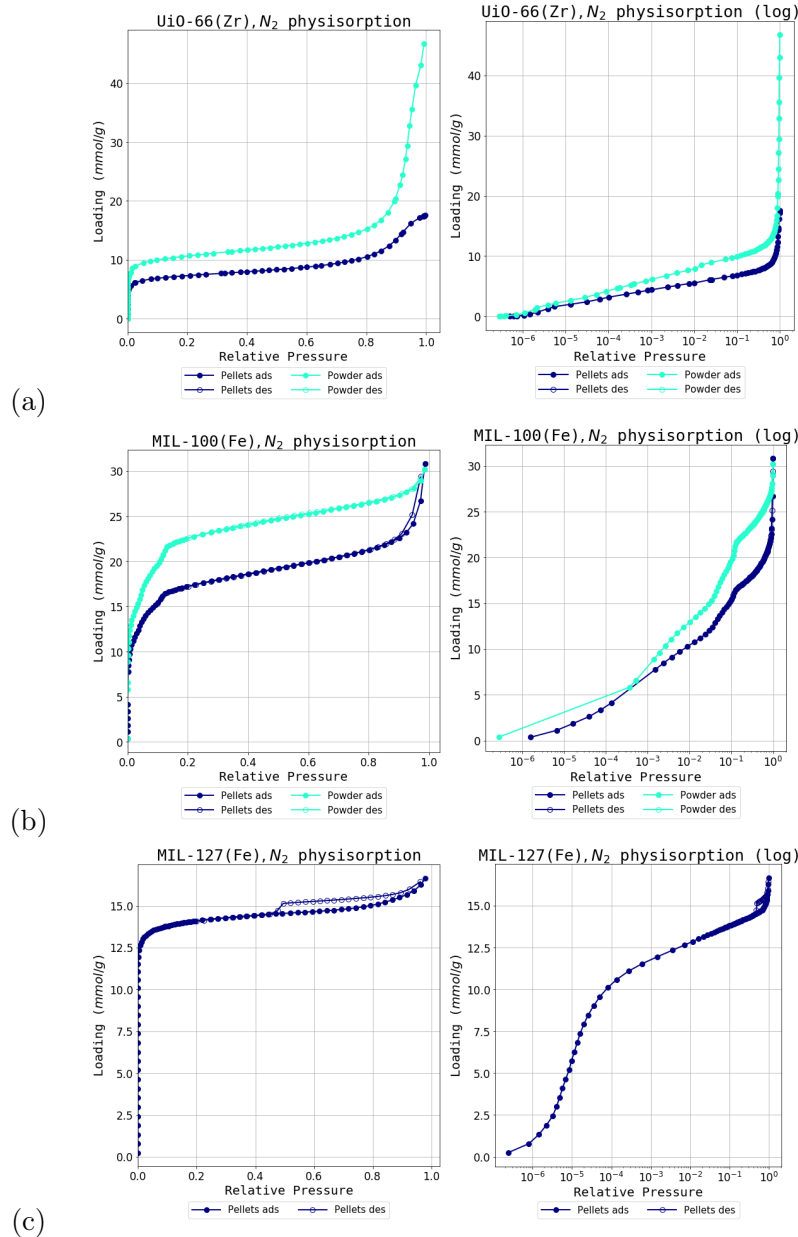


Figure 4.3.: Nitrogen isotherms at 77K for (a)  $\text{UiO-66}(\text{Zr})$ , (b)  $\text{MIL-100}(\text{Fe})$  and (c)  $\text{MIL-127}(\text{Fe})$ . The powder sample is in light blue while the  $\rho$ -alumina sample in dark blue. Logarithmic graphs of the isotherms are on the right for clarity of the low pressure region.

#### 4. Exploring the impact of material form on adsorption measurements

the corresponding powder. While in the case of MIL-127(Fe) the BET area is only 10% lower, for the MIL-100(Fe) and UiO-66(Zr) materials a larger drop is seen, of 25% and 31%, respectively. A similar decrease can be seen in pore volume, with a 36%, 23% and x% loss seen in UiO-66(Zr), MIL-100(Fe) and MIL-127(Fe) respectively. The decrease in both surface area and micropore volume is too large for it to be a consequence of the presence of non-porous binder. It is therefore theorised that some structure degradation must have occurred during the pelletisation process. Despite a loss in surface area, the bulk density of the material has increased, due to crystal aggregation.

some  
microp-  
ore vol-  
umes  
miss-  
ing +  
density

##### 4.4.3. Room temperature gas adsorption and microcalorimetry

As previously shown, combining microcalorimetry with adsorption manometry can give an insight into the energetics of the adsorption process by directly measuring differential heat. Even though the different contributions to the overall enthalpy curve cannot be decoupled from the individual sources, such as guest-host interactions or fluid-fluid interactions, it can be successfully applied to observing the effect of a process or treatment such as shaping on the properties of a MOF.

Eight probe gasses have been chosen for adsorption at 303 K: N<sub>2</sub>, CO, CO<sub>2</sub>, CH<sub>4</sub>, C<sub>2</sub>H<sub>6</sub>, C<sub>3</sub>H<sub>6</sub>, C<sub>3</sub>H<sub>8</sub> and C<sub>4</sub>H<sub>10</sub>. The range of adsorbates chosen allows different effects to be investigated. The adsorption of saturated hydrocarbons with an increasing carbon number (C1-C4) can be assumed to be driven strictly by Van-der-Waals forces, due to the shielding effects of the hydrogen atoms. Differences in the maximum uptakes of these gasses will point to loss of porosity or crystallinity. A capacity loss with an increasing carbon number will point to size exclusion effects induced by the binder, such as particle coating, pore filling or pore obstruction. The other probes have been chosen for their properties which can shine light on other specific interaction types present during the adsorption. Carbon monoxide is a slightly dipolar molecule which has the ability to act as an with other charges in the pores. It also can highlight CUS (coordinatively unsaturated sites) generated through defects, reduction or open metal sites due to its propensity for  $\pi$  backbonding coordination. This electron transfer process can also result in complexation with molecular orbitals in systems with  $\pi$  bonds such as alkenes and alkynes. Propylene is used as an unsaturated hydrocarbon probe gas for this purpose. Carbon dioxide is a highly quadrupolar molecule which will be strongly adsorbed in polar pore environments. Changes in the adsorption behaviour of CO<sub>2</sub> will shed light on such surface changes and can even be used as a predictor of hydrophobicity.<sup>(21)</sup> Finally, N<sub>2</sub> is a staple adsorbent for material characterisation when used at 77 K. The molecule is a slight quadrupole and has also been shown to chelate to some transitional metals in an analogue fashion to CO.

To eliminate the influence of kinetic and diffusion effects on the experiments, care has been taken to allow time for complete equilibration of both pressure and calorimeter signal. The complete dataset of adsorption isotherms, in the basis of both mass and volume can be found in Appendix C.

After collecting the combined isotherm and enthalpy data, three indicators have been chosen to best represent the effects of shaping: initial enthalpy of adsorption, initial

#### 4. Exploring the impact of material form on adsorption measurements

Henry constant and maximum capacity. These numeric performance indicators have been calculated using the available functionality in pyGAPS.

The initial enthalpy of adsorption extrapolated at zero coverage is a measure of the interaction with highest energetic sites on the MOF surface. Conversely, the initial Henry constant ( $K_H i$ ), here obtained through fitting the virial adsorption model through the method in ??, is also an indication of adsorption in the pores before any layering or adsorbate-adsorbate interaction comes into effect. The last indicator, maximum capacity, was taken as the loading attained when the isotherm reached a plateau. In the case of probes where the plateau was outside the range of pressure of the instrumentation (>50 bar), the loading at the highest available pressure was considered as a suitable approximation. The three key performance indicators (KPIs) have then been compared side by side on both the powder and shaped samples.

#### UiO-66(Zr)

A visual inspection of the enthalpy curves on as-synthesised UiO-66(Zr) show it to be relatively homogenous, with flat profiles being common. This is typical of this MOF, which has a pore environment without high energy adsorption sites.<sup>(16)</sup> Both CO<sub>2</sub> and CO show a higher enthalpy of adsorption at low loadings, as seen in Figure 4.4, which is likely due to their quadrupole and dipole interaction, respectively.

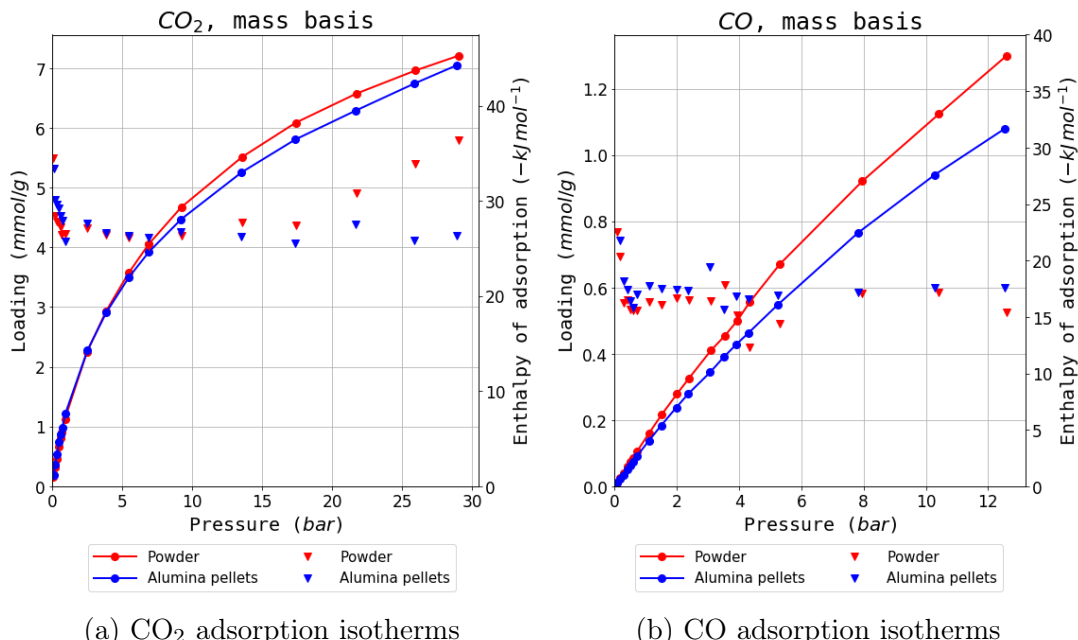


Figure 4.4.: Selected isotherms from the UiO-66(Zr) dataset

The KPI graphs in Figure 4.5 show very similar values for both Henry's constant and initial enthalpy of adsorption. It is therefore apparent that the shaping process did not change the interaction of the adsorbate with the MOF surface.

#### 4. Exploring the impact of material form on adsorption measurements

The maximum capacity graphs show a more interesting trend. When using small adsorbates such as N<sub>2</sub>, CO<sub>2</sub> and CH<sub>4</sub>, the shaped samples have a similar performance on a mass basis and, due to the densification process, better capacities on a volume basis. Starting with ethane, the maximum capacity difference starts to increase, with lower performance as molecule size increases. On hydrocarbons with a carbon number of 3 and 4, both mass basis and volume basis capacity is decreased compared to the original powder. This size exclusion effect could be explained by the coating of crystal surfaces with the alumina binder.

It could also be argued that instead of size exclusion, the effect is due to an overall decrease in pore volume, and that the isotherms of the low molecular weight gasses will diverge at higher pressures as the pores are filled. A counterargument for this hypothesis is that in the case of CO<sub>2</sub>, the plateau is reached with no differences between the powder and the pellet as seen in [Figure 4.4a](#).

Carbon monoxide is an apparent outlier to this trend, with a decreased maximum capacity and a small molecular size. However, when looking at the isotherms directly ([Figure 4.4b](#)) it is obvious that the effect is likely to be due to experimental errors, considering the low amount adsorbed and the good overlap in the enthalpy curves.

Overall, the shaping performance of UiO-66(Zr) is reasonable, as long as only small adsorbates are used.

#### MIL-100(Fe)

The enthalpy profiles on the MIL-100(Fe) powder are less homogenous than the ones on UiO-66(Zr). Some effects can be seen with probes which can interact with the partially reduced Fe(II) atom, such as carbon monoxide and propylene ([Figure 4.6](#)). Indeed, when comparing both the initial Henry constants and enthalpy of adsorption, for CO and C<sub>3</sub>H<sub>6</sub>, these are higher than the values obtained on UiO-66(Zr). With initial enthalpy of adsorption for CO of around 45 kJ mol<sup>-1</sup>, the value falls into the range of previous<sup>(18)</sup> results for interactions with such Fe(II) CUS.

Comparing the powder and shaped variants, there are no apparent differences between the two. The only discrepancy, which can be seen on the nitrogen initial  $K_H$  follows as a result of an ill-fitting virial parameter, and can be assumed an error after observing the isotherm overlap directly. It could be theorised that by activation at a higher temperature (250 °C), the percentage of iron trimers which would undergo reduction will increase and a further interaction could be observed. However, the activation temperature was chosen to allow comparisons with the PVA study,<sup>(14)</sup> where temperatures over 180 °C would lead to the burn-off of the polymer binder.

The maximum loading differences ([Figure 4.7c](#)) of MIL-100(Fe) show a very similar behaviour. On all probes tested, a fixed capacity loss of between 10-20% can be seen on a mass basis. However, the increase in density afforded by the compression during pelletisation leads to a compensation in performance as can be seen directly when looking at isotherms on mass and volume material basis in [Figure 4.6a](#) and [Figure 4.6b](#) respectively.

We can conclude that MIL-100(Fe) is almost unaffected by alumina shaping. A slight

#### 4. Exploring the impact of material form on adsorption measurements

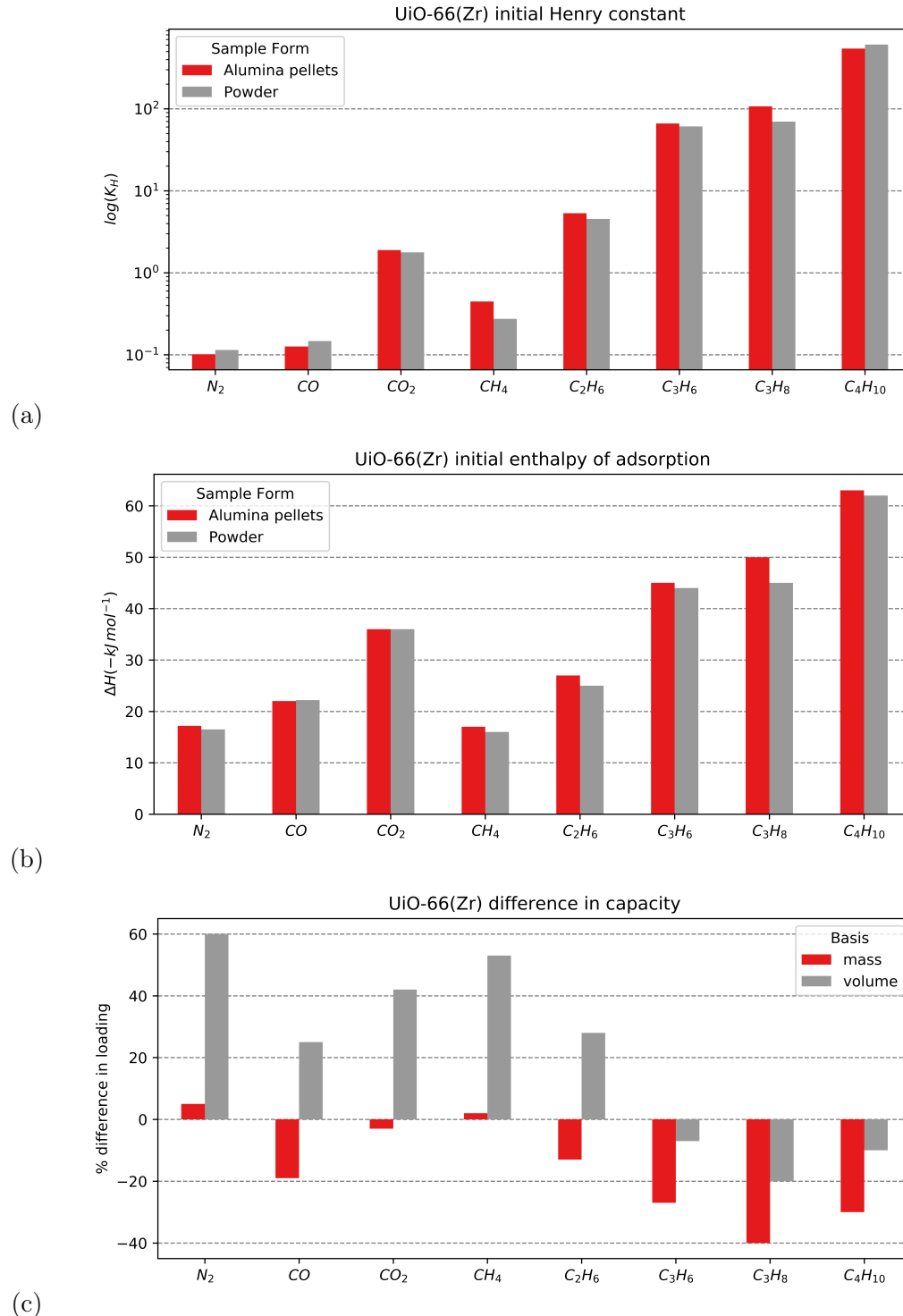


Figure 4.5.: KPIs extracted from the Uio-66(Zr) adsorption dataset with (a) logarithmic initial Henry constant (b) initial enthalpy of adsorption and (c) change in adsorption maximum capacity from the powder to the alumina shaped version on a mass and volume basis in red and grey respectively

#### 4. Exploring the impact of material form on adsorption measurements

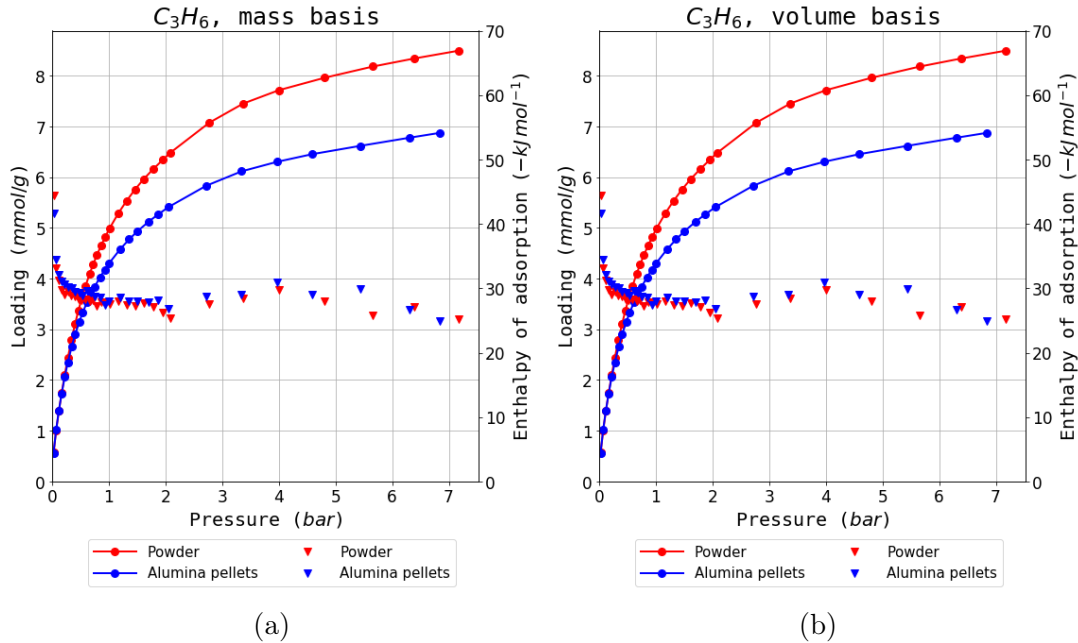


Figure 4.6.: Propylene isotherms on MIL-100(Fe) on a (a) mass and (b) volume adsorbent basis.

loss in maximum capacity on a mass basis is compensated by a pronounced densification, which is desirable in an industrial setting.

#### MIL-127(Fe)

The isotherms on the original powder form of MIL-127(Fe) should show similar behaviour as on MIL-100(Fe), due to the presence of the same iron trimesate moieties, although with a sharper uptake as a result of the smaller pores. Enthalpy profiles are also influenced by the similar interactions with the iron CUS leading to higher initial heats of adsorption on CO and C<sub>3</sub>H<sub>6</sub>. An overall increase in the heat of adsorption at higher loadings is seen throughout the probe series, as seen for example on butane in Figure 4.8a. Due to the bimodal pore distribution in the MIL-127(Fe) structure, it is likely that adsorption first commences in the small ( $\sim 6 \text{ \AA}$ ) channels and then, at higher pressures, intrusion into the larger cage-type pores is possible through the  $\sim 3 \text{ \AA}$  narrow apertures. The confined cages have an increased interaction with the molecule which leads to the higher enthalpy values.

When comparing the powder and the pellet variant with respect to initial Henry's constant, a large difference in  $K_H$  on CO stands out. The value of the initial enthalpy of adsorption does not follow the same pattern. However, visual inspection of the enthalpy curve in Figure 4.8b shows that the energy of adsorption corresponding to interactions with the more active sites is maintained for a larger percentage of the total coverage. This points to the higher preponderence of such sites in the powder variant. A similar offset can be seen in the propylene enthalpy at very low pressures, but this is not reflected

#### 4. Exploring the impact of material form on adsorption measurements

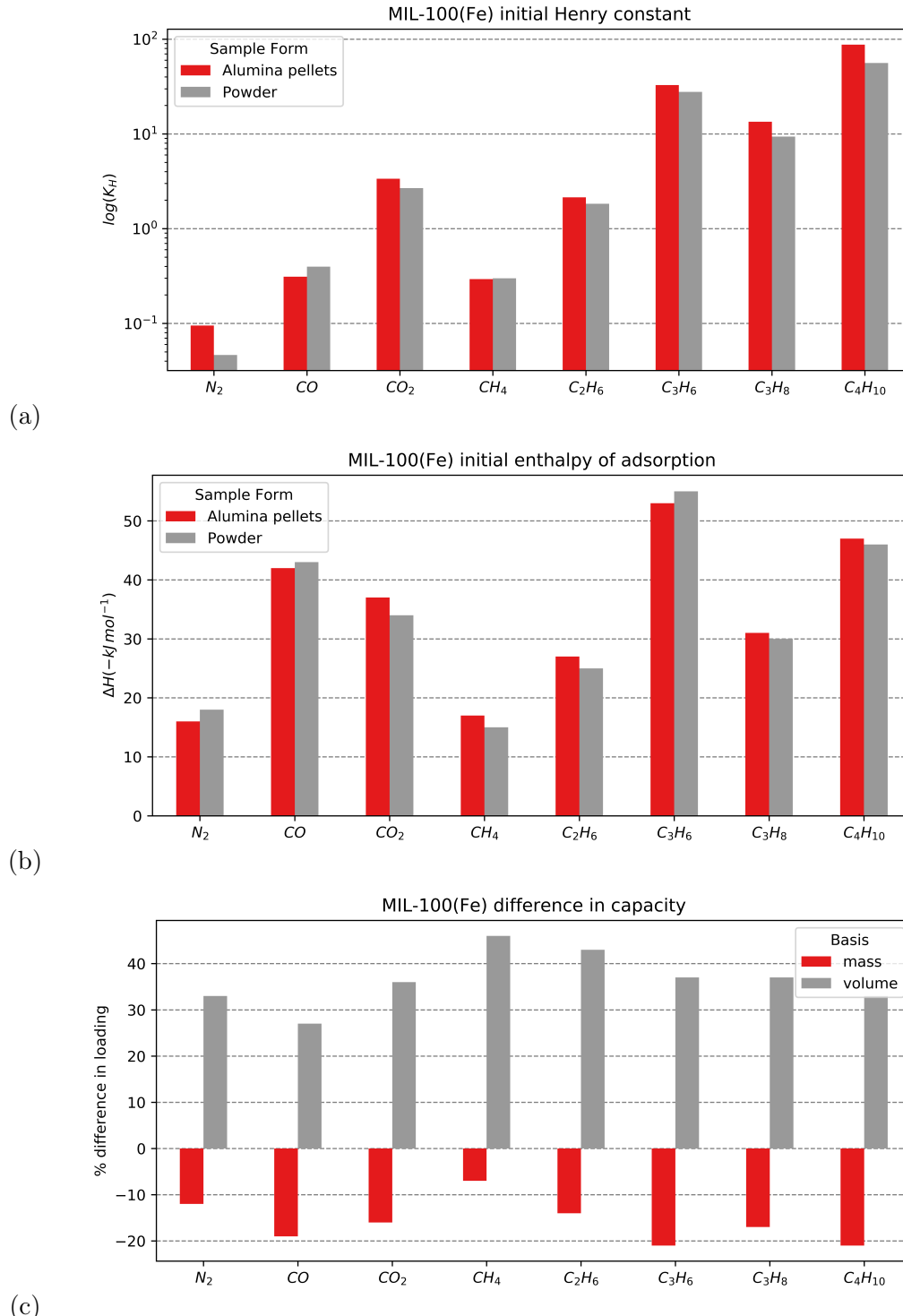


Figure 4.7.: KPIs extracted from the MIL-100(Fe) adsorption dataset with (a) logarithmic initial Henry constant (b) initial enthalpy of adsorption and (c) change in adsorption maximum capacity from the powder to the alumina shaped version on a mass and volume basis in red and grey respectively

#### 4. Exploring the impact of material form on adsorption measurements

in the shape of the isotherm. The weaker complexation strength and the larger size of the molecule likely limits the effect seen in the carbon monoxide isotherm. As for the underlying reason behind the isotherm divergence, it could be that the alumina binder acts as protection against the generation of iron(II) during thermal activation. No other differences are seen between the two forms on either Henry constant and initial enthalpy of adsorption.

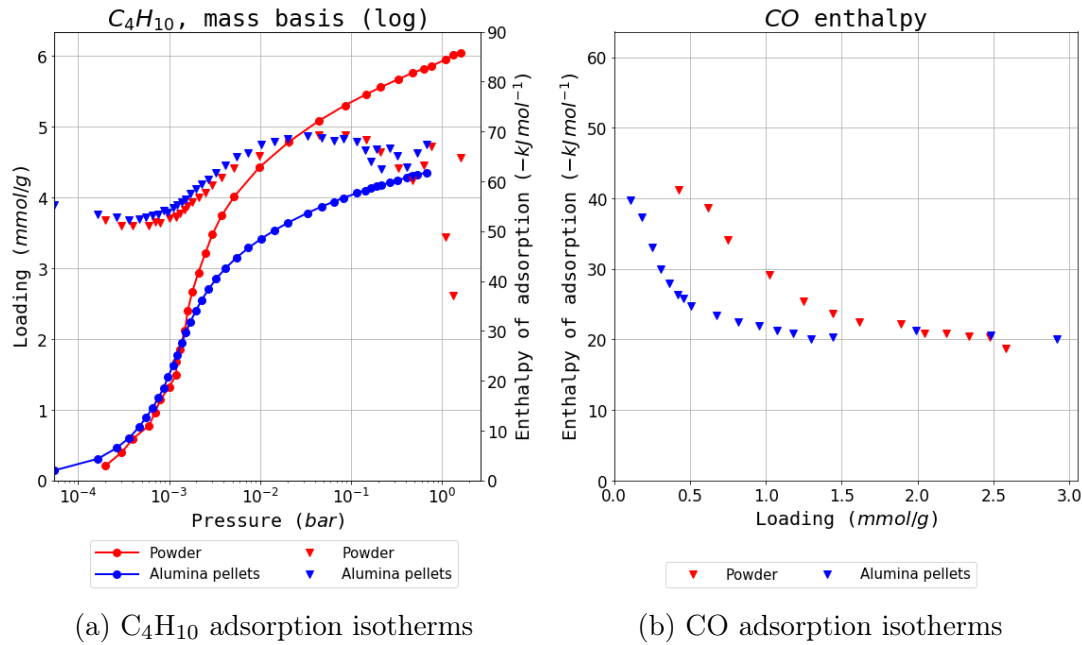


Figure 4.8.: Selected isotherms from the MIL-127(Fe) dataset

The capacity comparison in Figure 4.9c paints an interesting picture. For most probes there is no change in maximum loading showing that there is no structure degradation or pore filling. Two outliers are apparent: carbon monoxide and butane. The decrease in capacity on CO can be explained through the aforementioned changes in active site prevalence. The drop in butane cannot be a consequence of the same effect as there is a perfect overlap in the enthalpy curves as seen in Figure 4.8a. Therefore it likely better explained through a size exclusion effect as seen on UiO-66(Zr).

Overall, MIL-127(Fe) shows excellent performance when undergoing alumina shaping, with almost no capacity loss, as long as carbon monoxide or butane adsorption are required, where specific effects come into play.

#### 4.4.4. Vapour adsorption

The effects of shaping with  $\rho$ -alumina are so far more subtle than the changes encountered when using PVA, as shown in the corresponding study.<sup>(14)</sup> The influence of the binder on hydrophobic character of the material may be of interest for tuning the properties of the beads. Adsorption of water and methanol vapour can serve as a probe for

#### 4. Exploring the impact of material form on adsorption measurements

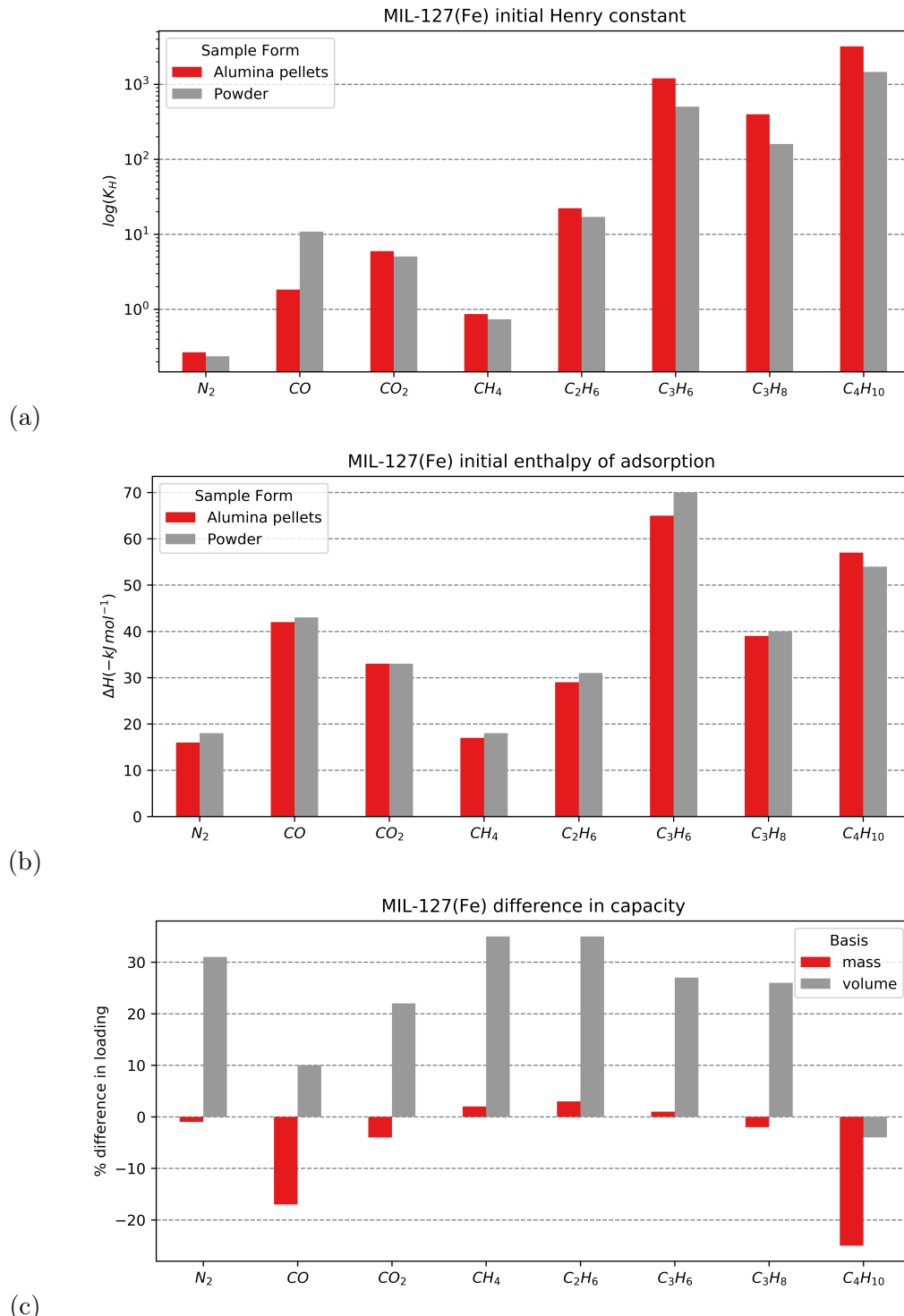


Figure 4.9.: KPIs extracted from the MIL-127(Fe) adsorption dataset with (a) logarithmic initial Henry constant (b) initial enthalpy of adsorption and (c) change in adsorption maximum capacity from the powder to the alumina shaped version on a mass and volume basis in red and grey respectively

#### 4. Exploring the impact of material form on adsorption measurements

small changes is surface properties. To this end, the same PVA samples which were studied in the previous study were studied alongside the MRA-shaped MOF.

Due to its surface charges, alumina is a hydrophilic substance, with a contact angle of 10°. It is expected that its addition will therefore increase the affinity of the resulting pellet towards water. On the other hand, the PVA binder is more hydrophilic, with a water contact angle of 51°. The medium affinity for water is due to the surface hydroxyl functionalizations, which can lead to hydrogen bonding.

Two indicators may highlight changes in material hydrophilicity: adsorption in the low relative pressure region ( $p/p^0 < 0.3$ ) and condensation steps in the isotherm. The adsorption at low pressures is representative of the first interactions with the surface, as explained in the previous sections. The pressure at which condensation occurs in the pores of the material, or where a sharp isotherm increase is seen depends on the size of the pore, but also on the pore environment and guest-guest interactions.

The measured isotherms on water and methanol can be found in [Figure 4.10](#) and [Figure 4.11](#) respectively. The isotherms measured on the original powder materials show the normal adsorption behaviour which can then be compared with the MRA and PVA shaped samples.

On UiO-66(Zr), the water isotherm shows a slow uptake at the start, corresponding to a hydrophobic material and then shows a small step at  $p/p^0 = 0.3$ . Complete pore filling happens at  $p/p^0 = 0.8$ .

Water isotherms on MIL-100(Fe) show a more hydrophilic environment, with a higher initial uptake, and two condensation steps at  $p/p^0 = 0.3$  and  $p/p^0 = 0.5$ . There is pronounced hysteresis on the desorption branch. The methanol adsorption isotherms also show a two step adsorption isotherm, but without any hysteresis present. The shaped samples also show a lower

It can be therefore concluded that overall, the addition of either binder has not influenced the behaviour towards water or methanol for the materials studied. The full water adsorption isotherms can be found in [Figure 4.10](#).

## 4.5. Conclusion

It can be concluded that the process of alumina shaping does not, in general, have an impact on the surface chemistry of the three MOF materials. Interestingly, in regards to the changes in maximum capacity, each material has its own particular behaviour: UiO-66(Zr) has a higher loss in capacity with larger molecular probes, MIL-100(Fe) has a decrease of 10-20% across all gasses and MIL-127(Fe) matches loading on a mass basis except on CO and C<sub>4</sub>H<sub>10</sub>.

The shaping also induces a densification which, in almost all cases, leads to a better performance on a volumetric basis. However, the influence on the mass transport effects of the alumina binder is not known and should be investigated further.

Overall, the process of alumina shaping is a promising method of preparing MOFs for gas-related applications in separation and storage, but care should be taken to not generalise the effects present on one material to another.

#### 4. Exploring the impact of material form on adsorption measurements

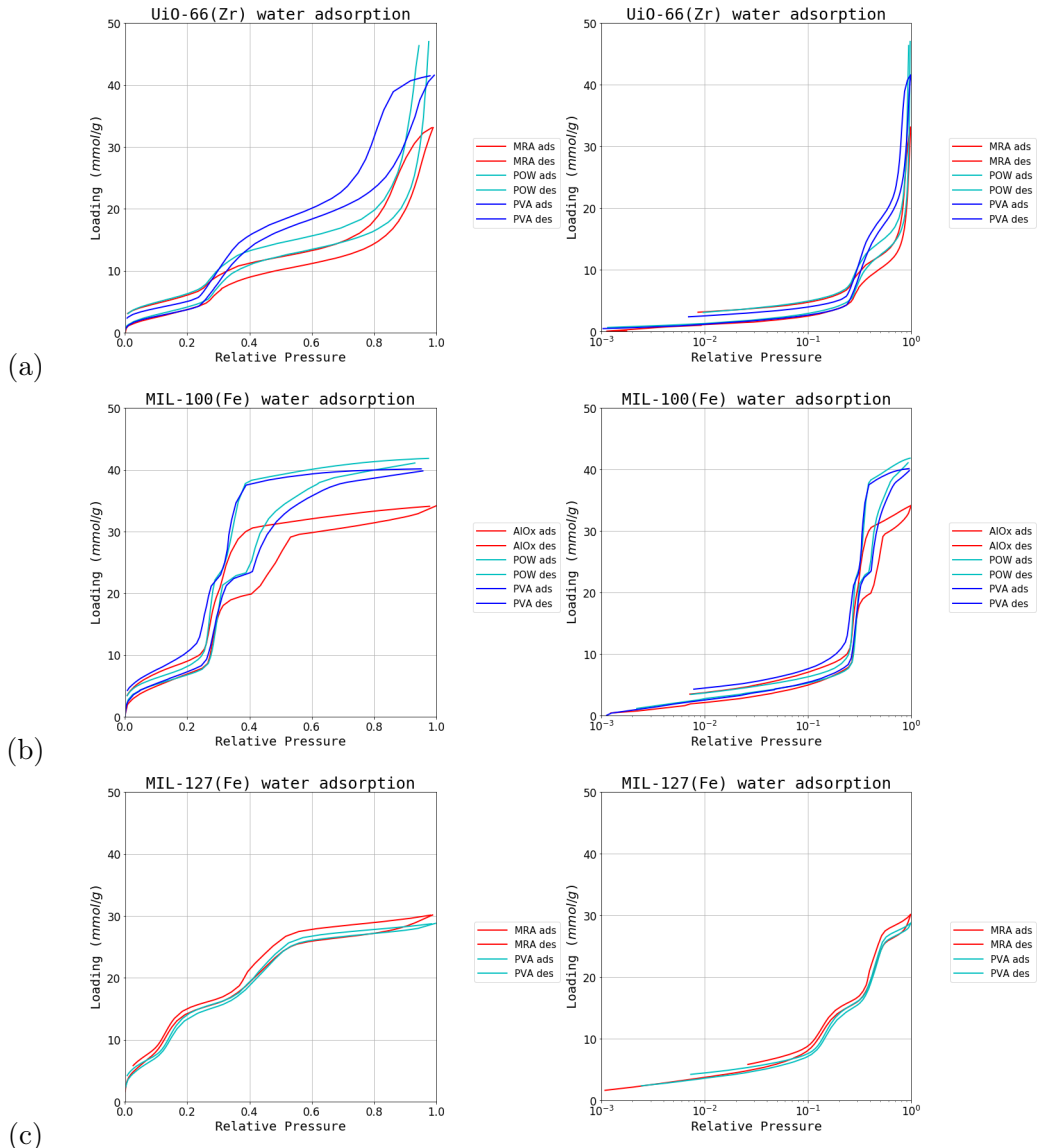


Figure 4.10.: Water adsorption isotherms (a) *UiO-66(Zr)*, (b) *MIL-100(Fe)* and (c) *MIL-127(Fe)*. The powder samples are in light blue, while the  $\rho$ -alumina and poly-vinyl alcohol samples are in red and dark blue respectively. Logarithmic graphs of the isotherms are on the right for clarity of the low pressure region.

#### 4. Exploring the impact of material form on adsorption measurements

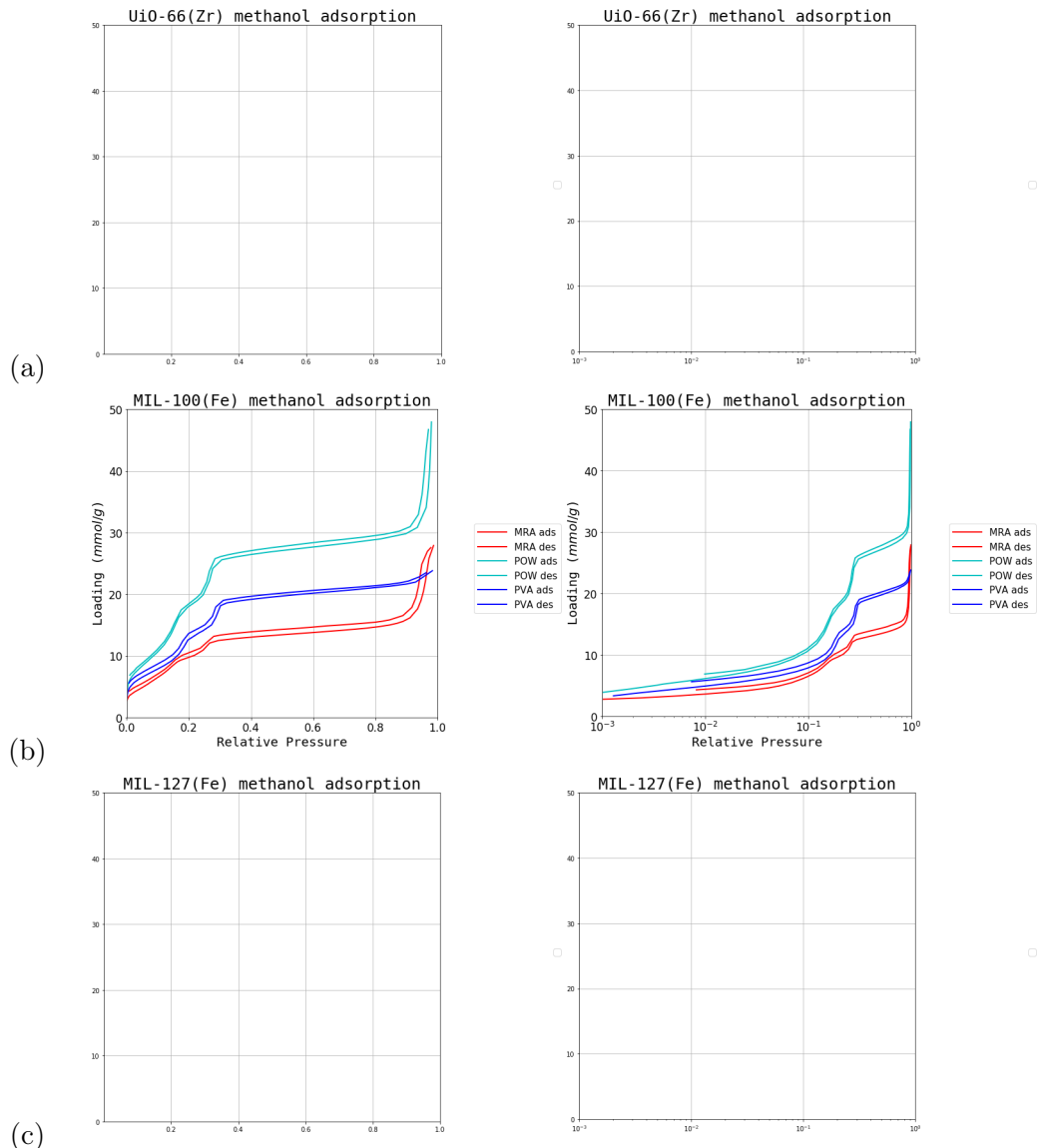


Figure 4.11.: Methanol adsorption isotherms (a)  $\text{UiO-66}(\text{Zr})$ , (b)  $\text{MIL-100}(\text{Fe})$  and (c)  $\text{MIL-127}(\text{Fe})$ . The powder samples are in light blue, while the  $\rho$ -alumina and poly-vinyl alcohol samples are in red and dark blue respectively. Logarithmic graphs of the isotherms are on the right for clarity of the low pressure region.

# Bibliography

- [1] Farid Akhtar, Linnéa Andersson, Steven Ogunwumi, Niklas Hedin, and Lennart Bergström. Structuring adsorbents and catalysts by processing of porous powders. *Journal of the European Ceramic Society*, 34(7):1643–1666, July 2014. ISSN 09552219. doi: 10.1016/j.jeurceramsoc.2014.01.008.
- [2] T. Ohji, M. Singh, J. A. Salem, Dongming Zhu, and American Ceramic Society, editors. *Advanced Processing and Manufacturing Technologies for Structural and Multifunctional Materials: A Collection of Papers Presented at the 31st International Conference on Advanced Ceramics and Composites, January 21-26, 2007, Daytona Beach, Florida*. Number v. 28, issue 7 in Ceramic engineering and science proceedings. Wiley-Interscience, Hoboken, N.J, 2008. ISBN 978-0-470-19638-0. OCLC: ocn154800301.
- [3] Teresa J. Bandosz, editor. *Activated Carbon Surfaces in Environmental Remediation*. Number 7 in Interface science and technology. Elsevier/AP, Amsterdam, 2006. ISBN 978-0-12-370536-5. OCLC: 255269962.
- [4] Douglas M. Ruthven. *Principles of Adsorption and Adsorption Processes*. Wiley, New York, 1984. ISBN 978-0-471-86606-0.
- [5] Gareth T. Whiting, Abhishek Dutta Chowdhury, Ramon Oord, Pasi Paalanen, and Bert M. Weckhuysen. The curious case of zeolite–clay/binder interactions and their consequences for catalyst preparation. *Faraday Discuss.*, 188:369–386, 2016. ISSN 1359-6640, 1364-5498. doi: 10.1039/C5FD00200A.
- [6] Nina-Luisa Michels, Sharon Mitchell, and Javier Pérez-Ramírez. Effects of Binders on the Performance of Shaped Hierarchical MFI Zeolites in Methanol-to-Hydrocarbons. *ACS Catalysis*, 4(8):2409–2417, August 2014. ISSN 2155-5435, 2155-5435. doi: 10.1021/cs500353b.
- [7] Stefan Kaskel, editor. *The Chemistry of Metal-Organic Frameworks: Synthesis, Characterization, and Applications*. Wiley-VCH Verlag GmbH & Co. KGaA, Weinheim, 2016. ISBN 978-3-527-69305-4 978-3-527-33874-0 978-3-527-69308-5 978-3-527-69306-1 978-3-527-69307-8.
- [8] Enrique V. Ramos-Fernandez, Mariana Garcia-Domingos, Jana Juan-Alcañiz, Jorge Gascon, and Freek Kapteijn. MOFs meet monoliths: Hierarchical structuring metal organic framework catalysts. *Applied Catalysis A: General*, 391(1-2):261–267, January 2011. ISSN 0926860X. doi: 10.1016/j.apcata.2010.05.019.
- [9] Sonia Aguado, Jerome Canivet, and David Farrusseng. Facile shaping of an imidazolate-based MOF on ceramic beads for adsorption and catalytic applications.

## Bibliography

- Chemical Communications*, 46(42):7999, 2010. ISSN 1359-7345, 1364-548X. doi: 10.1039/c0cc02045a.
- [10] D. Bazer-Bachi, L. Assié, V. Lecocq, B. Harbuzaru, and V. Falk. Towards industrial use of metal-organic framework: Impact of shaping on the MOF properties. *Powder Technology*, 255:52–59, March 2014. ISSN 00325910. doi: 10.1016/j.powtec.2013.09.013.
  - [11] Tian Tian, Jose Velazquez-Garcia, Thomas D. Bennett, and David Fairen-Jimenez. Mechanically and chemically robust ZIF-8 monoliths with high volumetric adsorption capacity. *Journal of Materials Chemistry A*, 3(6):2999–3005, 2015. ISSN 2050-7488, 2050-7496. doi: 10.1039/C4TA05116E.
  - [12] Rocio Semino, Naseem A. Ramsahye, Aziz Ghoufi, and Guillaume Maurin. Microscopic Model of the Metal–Organic Framework/Polymer Interface: A First Step toward Understanding the Compatibility in Mixed Matrix Membranes. *ACS Applied Materials & Interfaces*, 8(1):809–819, January 2016. ISSN 1944-8244, 1944-8252. doi: 10.1021/acsami.5b10150.
  - [13] Takashi Kitao, Yuanyuan Zhang, Susumu Kitagawa, Bo Wang, and Takashi Uemura. Hybridization of MOFs and polymers. *Chemical Society Reviews*, 46(11): 3108–3133, 2017. ISSN 0306-0012. doi: 10.1039/C7CS00041C.
  - [14] Nicolas Chanut, Andrew D. Wiersum, U-Hwang Lee, Young Kyu Hwang, Florence Ragon, Hubert Chevreau, Sandrine Bourrelly, Bogdan Kuchta, Jong-San Chang, Christian Serre, and Philip L. Llewellyn. Observing the Effects of Shaping on Gas Adsorption in Metal-Organic Frameworks. *European Journal of Inorganic Chemistry*, 2016(27):4416–4423, September 2016. ISSN 14341948. doi: 10.1002/ejic.201600410.
  - [15] Jasmina Hafizovic Cavka, Søren Jakobsen, Unni Olsbye, Nathalie Guillou, Carlo Lamberti, Silvia Bordiga, and Karl Petter Lillerud. A New Zirconium Inorganic Building Brick Forming Metal Organic Frameworks with Exceptional Stability. *Journal of the American Chemical Society*, 130(42):13850–13851, October 2008. ISSN 0002-7863. doi: 10.1021/ja8057953.
  - [16] Andrew D. Wiersum, Estelle Soubeyrand-Lenoir, Qingyuan Yang, Beatrice Moulin, Vincent Guillerm, Mouna Ben Yahia, Sandrine Bourrelly, Alexandre Vimont, Stuart Miller, Christelle Vagner, Marco Daturi, Guillaume Clet, Christian Serre, Guillaume Maurin, and Philip L. Llewellyn. An Evaluation of UiO-66 for Gas-Based Applications. *Chemistry - An Asian Journal*, 6(12):3270–3280, December 2011. ISSN 18614728. doi: 10.1002/asia.201100201.
  - [17] Patricia Horcajada, Suzy Surblé, Christian Serre, Do-Young Hong, You-Kyong Seo, Jong-San Chang, Jean-Marc Grenèche, Irene Margiolaki, and Gérard Férey. Synthesis and catalytic properties of MIL-100(Fe), an iron( III ) carboxylate with large

## Bibliography

- pores. *Chem. Commun.*, (27):2820–2822, 2007. ISSN 1359-7345, 1364-548X. doi: 10.1039/B704325B.
- [18] Ji Woong Yoon, You-Kyong Seo, Young Kyu Hwang, Jong-San Chang, Hervé Leclerc, Stefan Wuttke, Philippe Bazin, Alexandre Vimont, Marco Daturi, Emily Bloch, Philip L. Llewellyn, Christian Serre, Patricia Horcajada, Jean-Marc Grenèche, Alirio E. Rodrigues, and Gérard Férey. Controlled Reducibility of a Metal-Organic Framework with Coordinatively Unsaturated Sites for Preferential Gas Sorption. *Angewandte Chemie International Edition*, 49(34):5949–5952, August 2010. ISSN 14337851. doi: 10.1002/anie.201001230.
- [19] Yunling Liu, Jarrod F. Eubank, Amy J. Cairns, Juergen Eckert, Victor Ch. Kravtsov, Ryan Luebke, and Mohamed Eddaoudi. Assembly of Metal-Organic Frameworks (MOFs) Based on Indium-Trimer Building Blocks: A Porous MOF with  $\text{soc}$  Topology and High Hydrogen Storage. *Angewandte Chemie International Edition*, 46(18):3278–3283, April 2007. ISSN 14337851, 15213773. doi: 10.1002/anie.200604306.
- [20] Hubert Chevreau, Anastasia Permyakova, Farid Nouar, Paul Fabry, Carine Livage, Florence Ragon, Alfonso Garcia-Marquez, Thomas Devic, Nathalie Steunou, Christian Serre, and Patricia Horcajada. Synthesis of the biocompatible and highly stable MIL-127(Fe): From large scale synthesis to particle size control. *CrystEngComm*, 18(22):4094–4101, 2016. ISSN 1466-8033. doi: 10.1039/C5CE01864A.
- [21] Nicolas Chanut, Sandrine Bourrelly, Bogdan Kuchta, Christian Serre, Jong-San Chang, Paul A. Wright, and Philip L. Llewellyn. Screening the Effect of Water Vapour on Gas Adsorption Performance: Application to CO<sub>2</sub> Capture from Flue Gas in Metal-Organic Frameworks. *ChemSusChem*, 10(7):1543–1553, April 2017. ISSN 18645631. doi: 10.1002/cssc.201601816.
- [22] Qingyuan Yang, Sébastien Vaesen, Florence Ragon, Andrew D. Wiersum, Dong Wu, Ana Lago, Thomas Devic, Charlotte Martineau, Francis Taulelle, Philip L. Llewellyn, Hervé Jobic, Chongli Zhong, Christian Serre, Guy De Weireld, and Guillaume Maurin. A Water Stable Metal-Organic Framework with Optimal Features for CO<sub>2</sub> Capture. *Angewandte Chemie*, 125(39):10506–10510, September 2013. ISSN 00448249. doi: 10.1002/ange.201302682.
- [23] Anil H. Valekar, Kyung-Ho Cho, U-Hwang Lee, Ji Sun Lee, Ji Woong Yoon, Young Kyu Hwang, Seung Gwan Lee, Sung June Cho, and Jong-San Chang. Shaping of porous metal-organic framework granules using mesoporous  $\rho$ -alumina as a binder. *RSC Advances*, 7(88):55767–55777, 2017. ISSN 2046-2069. doi: 10.1039/C7RA11764G.

# A. Common characterisation techniques

## A.1. Thermogravimetry

Thermogravimetry (TGA) is a standard laboratory technique where the weight of a sample is monitored while ambient temperature is controlled. Changes in sample mass can be correlated to physical events, such as adsorption, desorption, sample decomposition or oxidation, depending on temperature and its rate of change.

TGA experiments are carried out on approximately 15 mg of sample with a TA Instruments Q500 up to 800 °C. The sample is placed on a platinum crucible and sealed in a temperature controlled oven, under gas flow of  $40 \text{ cm}^3 \text{ min}^{-1}$ . Experiments can use a blanket of either air or argon. The temperature ramp can be specified directly and should be chosen to ensure that the sample is in equilibrium with the oven temperature and no thermal conductivity effects come into play. Alternatively, a dynamic “Hi-Res” mode can be used which allows for automatic cessation of heating rate while the sample undergoes mass loss.

The main purpose of thermogravimetry as used in this thesis is the determination of sample decomposition temperature, to ensure that thermal activation prior to adsorption is complete and that all guest molecules have been removed without loss of structure. To this end, experiments are performed under an inert atmosphere (argon), and the sample activation temperature is chosen as 50 °C to 100 °C lower than the sample decomposition temperature.

## A.2. Bulk density determination

Bulk density is a useful metric for the industrial use of adsorbent materials, as their volume plays a critical role in equipment sizing.

Bulk density is determined by weighing 1.5 ml empty glass vessels and settling the MOFs inside. Powder materials are then added in small increments and settled through vibration between each addition. The full vessel is finally weighed, which allowed the bulk density to be determined. The same cell is used in all experiments, with cleaning through sonication between each experiment.

## A.3. Skeletal density determination

True density or skeletal density is determined through gas pycnometry in a Microtrac-BEL BELSORP-max apparatus. Helium is chosen as the fluid of choice as it is assumed to be non-adsorbing.

## A. Common characterisation techniques

The volume of a glass sample cell ( $V_c$ ) is precisely measured through dosing of the reference volume with helium up to ( $p_1$ ), then opening the valve connecting the two and allowing the gas to expand up to ( $p_2$ ). Afterwards approximately 50 mg of sample are weighed and inserted in a glass sample cell. After sample activation using the supplied electric heater to ensure no solvent residue is left in the pores, the same procedure is repeated to determine the volume of the cell and the adsorbent. With the volume of the sample determined, the density can be calculated by.

$$V_s = V_c + \frac{V_r}{1 - \frac{p_1}{p_2}} \quad (\text{A.1})$$

### A.4. Nitrogen physisorption at 77 K

Nitrogen adsorption experiments are carried out on a Micromeritics Triflex apparatus. Approximately 60 mg of sample are used for each measurement. Empty glass cells are weighed and filled with the samples, which are then activated in a Micromeritics Smart VacPrep up to their respective activation temperature under vacuum and then back-filled with an inert atmosphere. After sample activation, the cells are re-weighed to determine the precise sample mass. The cells are covered with a porous mantle which allows for a constant temperature gradient during measurement by wicking liquid nitrogen around the cell. Finally, the cells are immersed in a liquid nitrogen bath and the adsorption isotherm is recorded using the volumetric method. A separate cell is used to condense the adsorptive throughout the measurement for accurate determination of its saturation pressure.

### A.5. Vapour physisorption at 298 K

Vapour adsorption isotherms throughout this work are measured using a MicrotracBEL BELSORP-max apparatus in vapour mode. Glass cells are first weighed and then filled with about 50 mg of sample. The vials are then heated under vacuum up to the activation temperature of the material and re-weighed in order to measure the exact sample mass without adsorbed guests. The cells are then immersed in a mineral oil bath kept at 298 K. To ensure that the cold point of the system occurs in the material and to prevent condensation on cell walls, the reference volume, dead space and vapour source are temperature controlled through an insulated enclosure.

### A.6. Gravimetric isotherms

The gravimetric isotherms in this thesis are obtained using a commercial Rubotherm GmbH balance. Approximately 1 g of dried sample is used for these experiments. Samples are activated *in situ* by heating under vacuum. The gas is introduced using a

### *A. Common characterisation techniques*

step-by-step method, and equilibrium is assumed to have been reached when the variation of weight remained below 30 µg over a 15 min interval. The volume of the sample is determined from a blank experiment with helium as the non-adsorbing gas and used in combination with the gas density measured by the Rubotherm balance to compensate for buoyancy.

# B.Synthesis method of referenced materials

## B.1. Takeda 5A reference carbon

The Takeda 5A carbon was purchased directly from the Takeda corporation. The sample was activated at 250 °C under secondary vacuum (5 mbar) before any measurements.

full  
char-  
acteri-  
zation

## B.2. MCM-41 controlled pore glass

MCM-41 (Mobil Composition of Matter No. 41) is a mesoporous silica ( $\text{SiO}_2$ ) material with a narrow pore distribution. First synthesised by the Mobil Oil Corporation, it is produced through templated synthesis using mycelle-forming surfactants. The material referenced in this thesis was purchased from Sigma-Aldrich. The activation procedure consists of heating at 250 °C under secondary vacuum (5 mbar).

## B.3. Zr fumarate MOF

The synthesis of the Zr fumarate was performed in Peter Behren's group in Hannover, through modulated synthesis. This MOF can only be synthesised through the addition of a modulator, in this case fumaric acid, to the ongoing reactor, as detailed in the original publication.<sup>(?)</sup>

The procedure goes as follows:  $\text{ZrCl}_4$  (0.517 mmol, 1 eq) and fumaric acid (1.550 mmol, 3 eq) are dissolved in 20 mL N,N-dimethylformamide (DMF) and placed in a 100 mL glass flask at room temperature. 20 equivalents of formic acid were added. The glass flasks were Teflon-capped and heated in an oven at 120 °C for 24 h. After cooling, the white precipitate was washed with 10 mL DMF and 10 mL ethanol, respectively. The washing process was carried out by centrifugation and redispersion of the white powder, which was then dried at room temperature over night

## B.4. UiO-66(Zr) for defect study

The UiO-66(Zr) sample preparation was adapted from Shearer et al. <sup>(?)</sup> as follows:  $\text{ZrCl}_4$  (1.55 g, 6.65 mmol), an excess of terephthalic acid (BDC) (1.68 g, 10.11 mmol), HCl 37 % solution (0.2 mL, 3.25 mmol) and N,N'-dimethylformamide (DMF) (200 mL, 2.58 mol) were added to a 250 mL pressure resistant Schott bottle. The mixture was stirred for 10 min, followed by incubation in a convection oven at 130 °C for 24 h. The resulting white precipitate was washed with fresh DMF (3× 50 mL) followed by ethanol (3× 50 mL) over the course of 48 h and dried at 60 °C. After drying, the sample was

### *B. Synthesis method of referenced materials*

activated on a vacuum oven by heating at 200 °C under vacuum for 12 h. The yield was 78 % white microcrystalline powder. Before the experiment, the sample was calcined at 200 °C under vacuum (5 mbar) to remove any residual solvents from the framework.

## **B.5. UiO-66(Zr) for shaping study**

The scaled-up synthesis of UiO-66(Zr) was carried out in a 5 L glass reactor (Reactor Master, Syrris, equipped with a reflux condenser and a Teflon-lined mechanical stirrer) according to a previously reported method.<sup>(?)</sup> In short, 462 g (2.8 mol) of H<sub>2</sub>BDC (98%) was initially dissolved in 2.5 L of dimethyl formamide (DMF, 2.36 kg, 32.3 mol) at room temperature. Then, 896 g (2.8 mol) of ZrOCl<sub>2</sub> · 8H<sub>2</sub>O (98%) and 465 mL of 37% HCl (548 g, 15 mol) were added to the mixture. The molar ratio of the final ZrOCl<sub>2</sub> · 8H<sub>2</sub>O/H<sub>2</sub>BDC/DMF/HCl mixture was 1 : 1 : 11.6 : 5.4. The reaction mixture was vigorously stirred to obtain a homogeneous gel. The mixture was then heated to 423 K at a rate of 1 K min<sup>-1</sup> and maintained at this temperature for 6 h in the reactor without stirring, leading to a crystalline UiO-66(Zr) solid. The resulting product (510 g) was recovered from the slurry by filtration, redispersed in 7 L of DMF at 333 K for 6 h under stirring, and recovered by filtration. The same procedure was repeated twice, using methanol (MeOH) instead of DMF. The solid product was finally dried at 373 K overnight.

## **B.6. MIL-100(Fe) for shaping study**

The synthesis of the MOF for the shaping study was done at the KRICT institute using a previously published method.<sup>(?)</sup> To synthesise the MIL-100(Fe) material Fe(NO<sub>3</sub>)<sub>3</sub> was completely dissolved in water. Then, trimesic acid (BTC) was added to the solution; the resulting mixture was stirred at room temperature for 1 h. The final composition was Fe(NO<sub>3</sub>)<sub>3</sub> · 9 H<sub>2</sub>O : 0.67 BTC : n H<sub>2</sub>O (x = 55–280). The reactant mixture was heated at 433 K for 12 h using a Teflon-lined pressure vessel. The synthesized solid was filtered and washed with deionized (DI) water. Further washing was carried out with DI water and ethanol at 343 K for 3 h and purified with a 38 mM NH<sub>4</sub>F solution at 343 K for 3 h. The solid was finally dried overnight at less than 373 K in air.

## **B.7. MIL-127(Fe) for shaping study**

MIL-127(Fe) was synthesized by reaction of Fe(ClO<sub>4</sub>)<sub>3</sub> · 6 H<sub>2</sub>O (3.27 g, 9.2 mmol) and C<sub>16</sub>N<sub>2</sub>O<sub>8</sub>H<sub>6</sub> (3.3 g) in DMF (415 mL) and hydrofluoric acid (5 M, 2.7 mL) at 423 K in a Teflon flask. The obtained orange crystals were placed in DMF (100 mL) and stirred at ambient temperature for 5 h. The final product was kept at 375 K overnight. MIL-127(Fe) was synthesized by reaction of Fe(ClO<sub>4</sub>)<sub>3</sub> · 6 H<sub>2</sub>O (3.27 g, 9.2 mmol) and C<sub>16</sub>N<sub>2</sub>O<sub>8</sub>H<sub>6</sub> (3.3 g) in DMF (415 mL) and hydrofluoric acid (5 M, 2.7 mL) at 423 K in a Teflon flask.

*B. Synthesis method of referenced materials*

The obtained orange crystals were placed in DMF (100 mL) and stirred at ambient temperature for 5 h. The final product was kept at 375 K overnight.

# C. Complete adsorption dataset for shaping study

## C.1. Calorimetry dataset UiO-66(Zr)

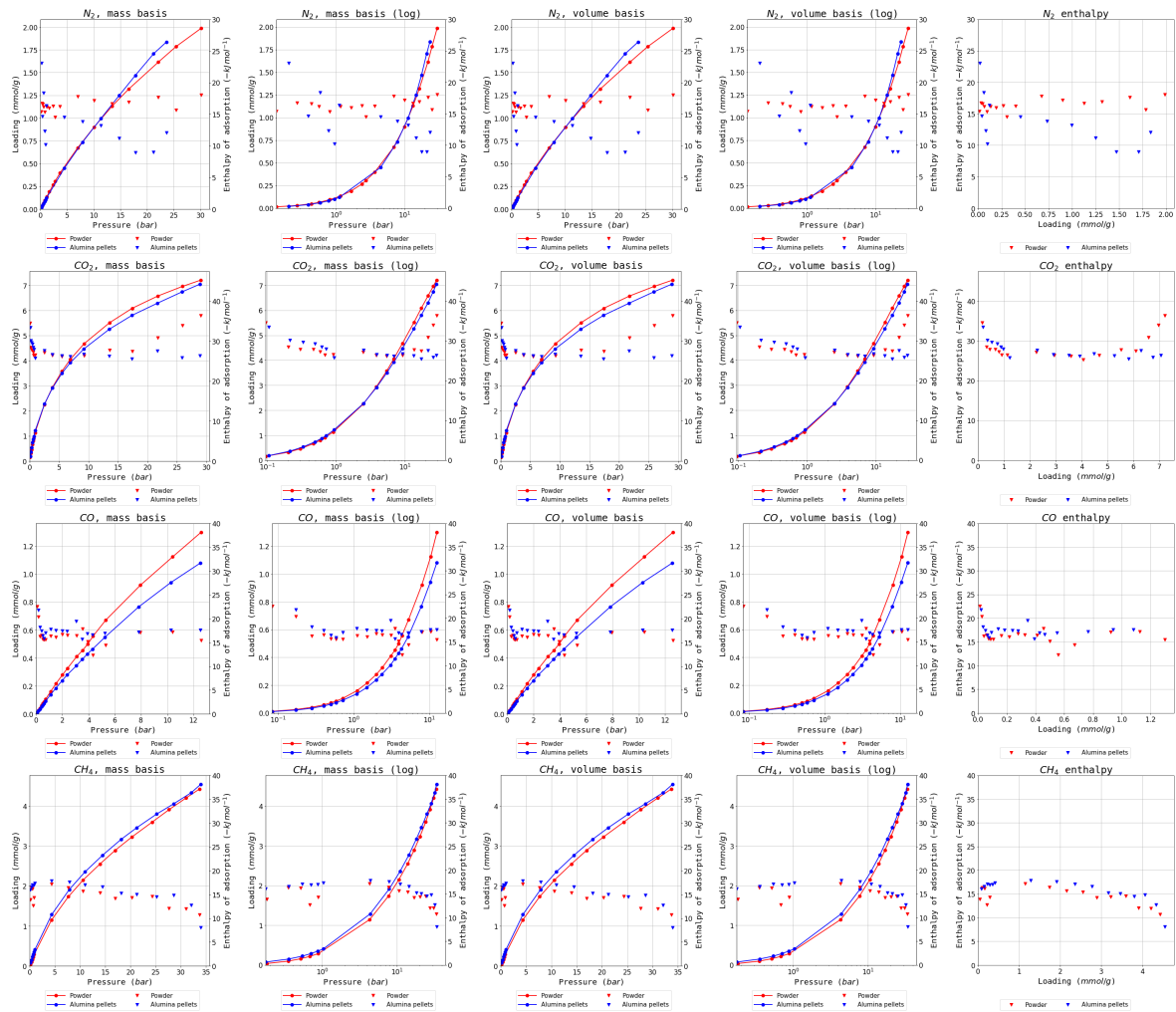


Figure C.1.: Complete isotherm and enthalpy dataset for UiO-66(Zr)

### C. Complete adsorption dataset for shaping study

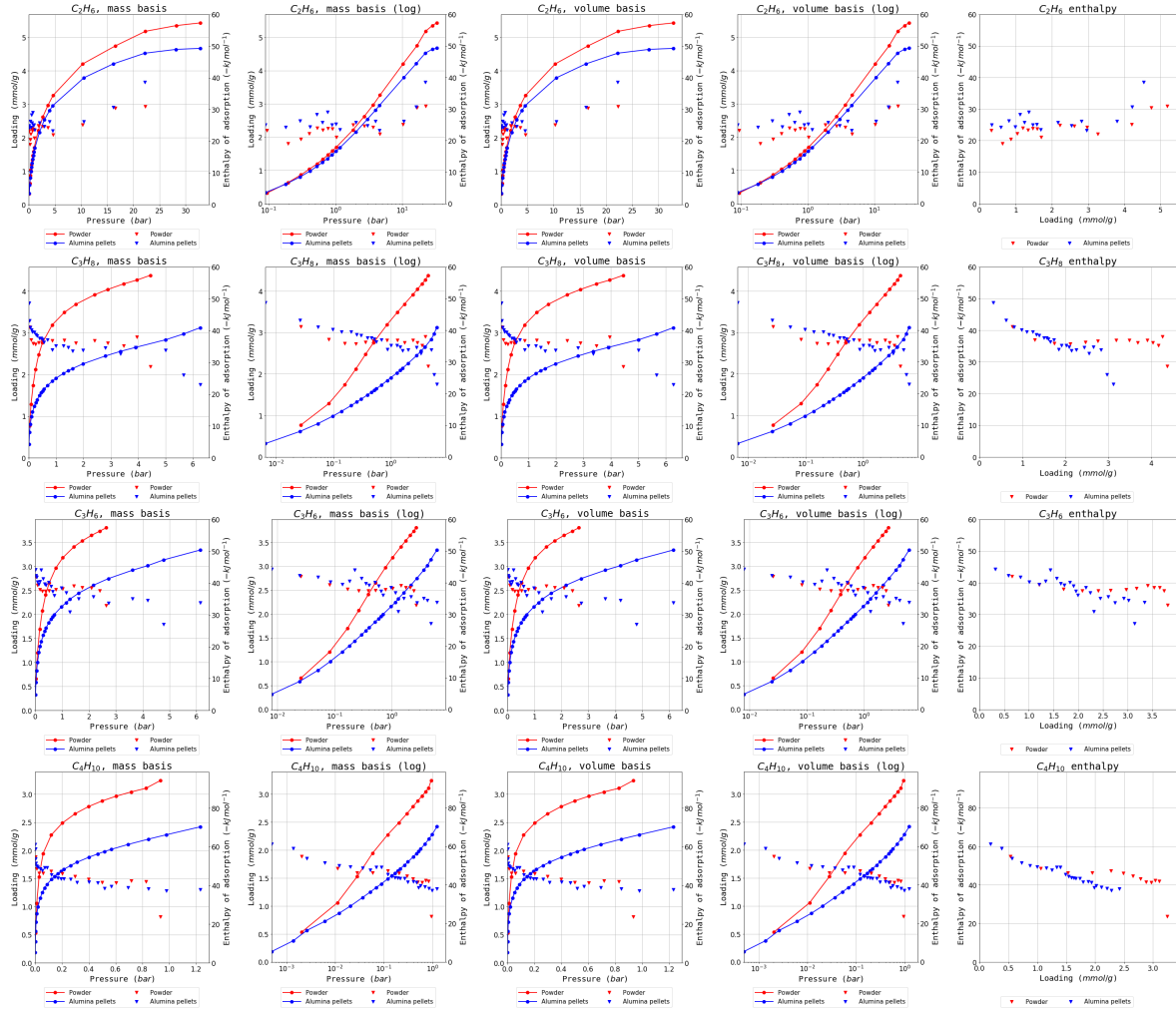


Figure C.1.: Complete isotherm and enthalpy dataset for UiO-66(Zr)

### C.2. Calorimetry MIL-100(Fe)

### C. Complete adsorption dataset for shaping study

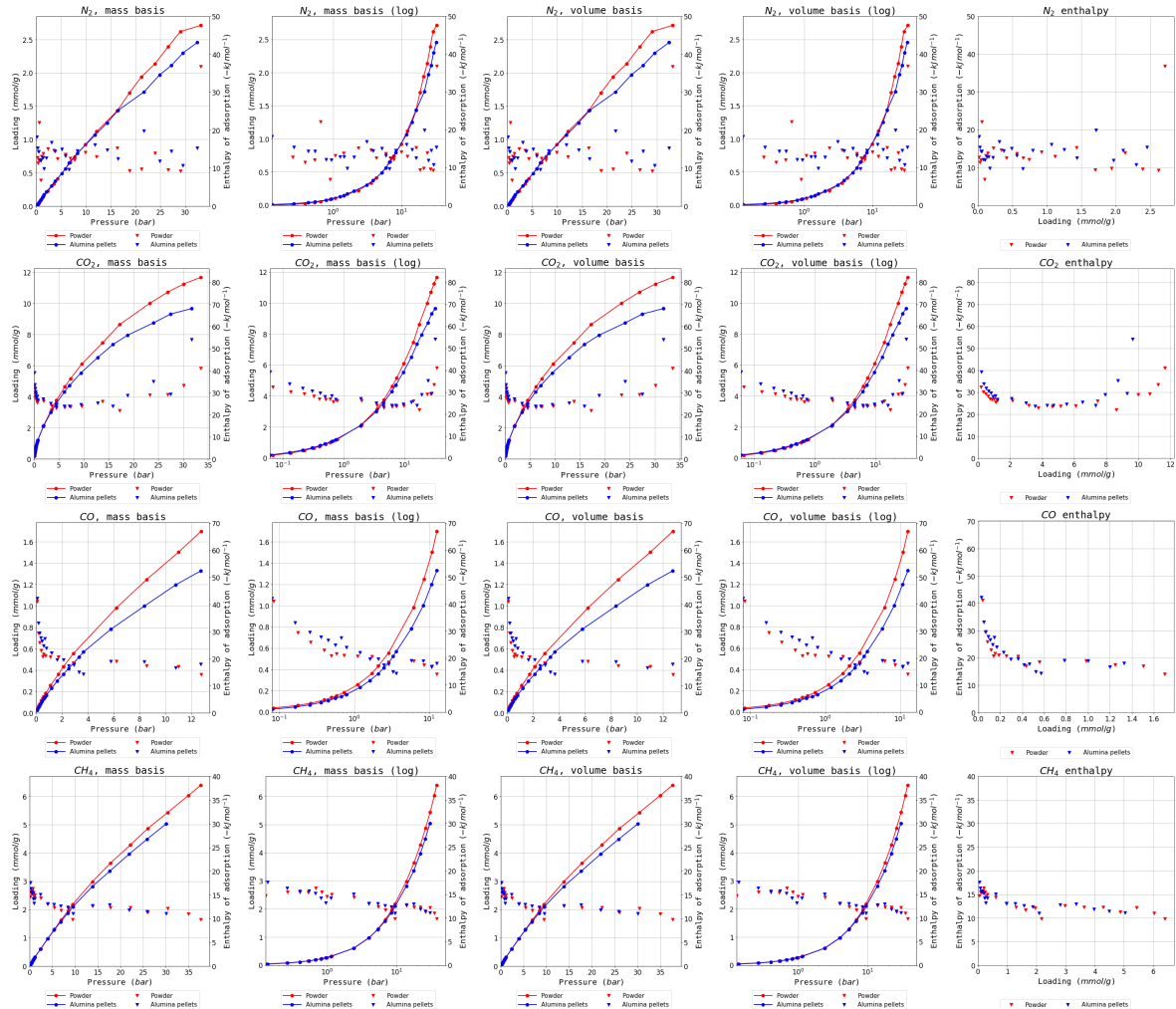


Figure C.2.: Complete isotherm and enthalpy dataset for MIL-100(Fe)

### C. Complete adsorption dataset for shaping study

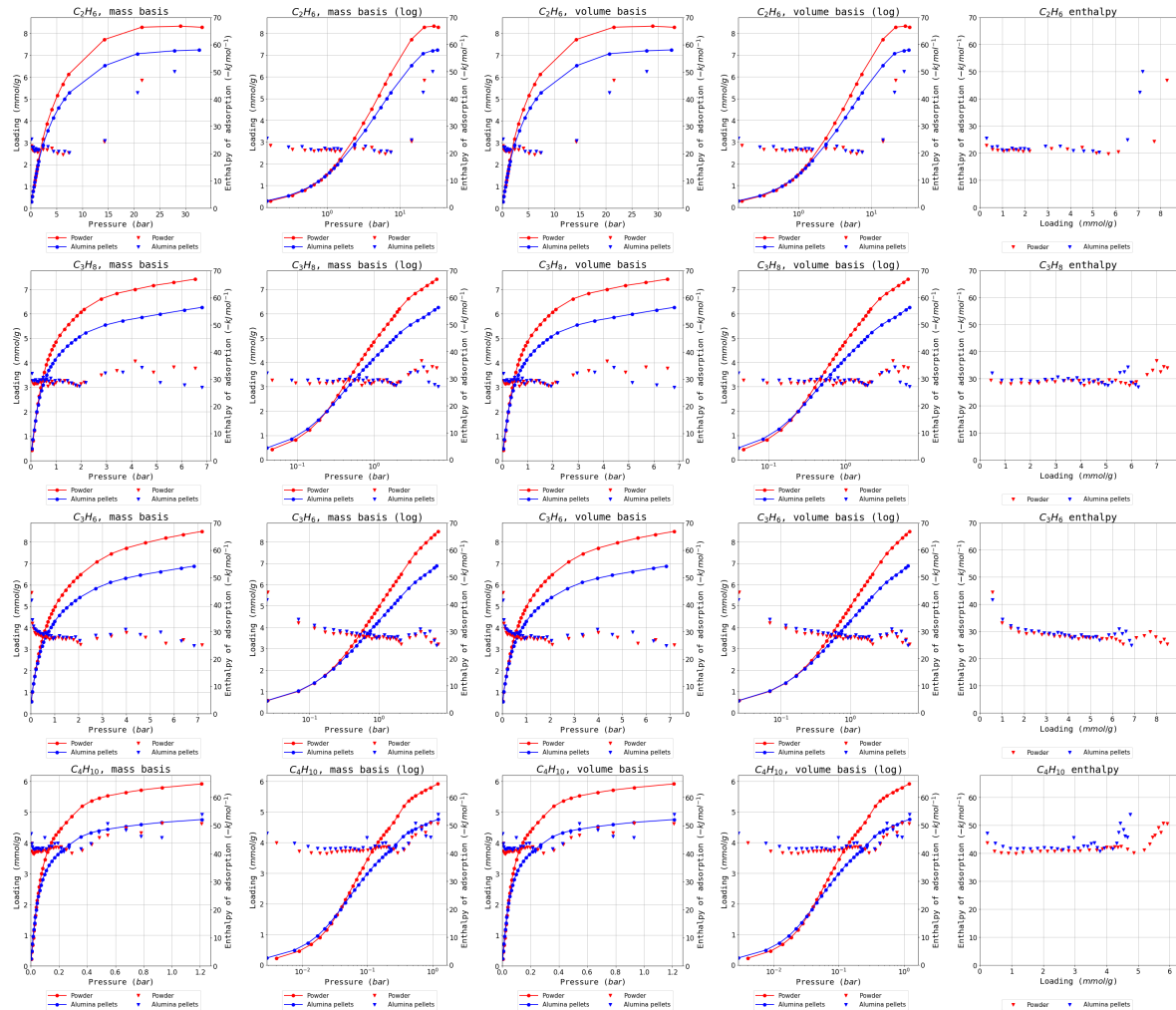


Figure C.2.: Complete isotherm and enthalpy dataset for MIL-100(Fe)

### C. Complete adsorption dataset for shaping study

#### C.3. Calorimetry MIL-127(Fe)

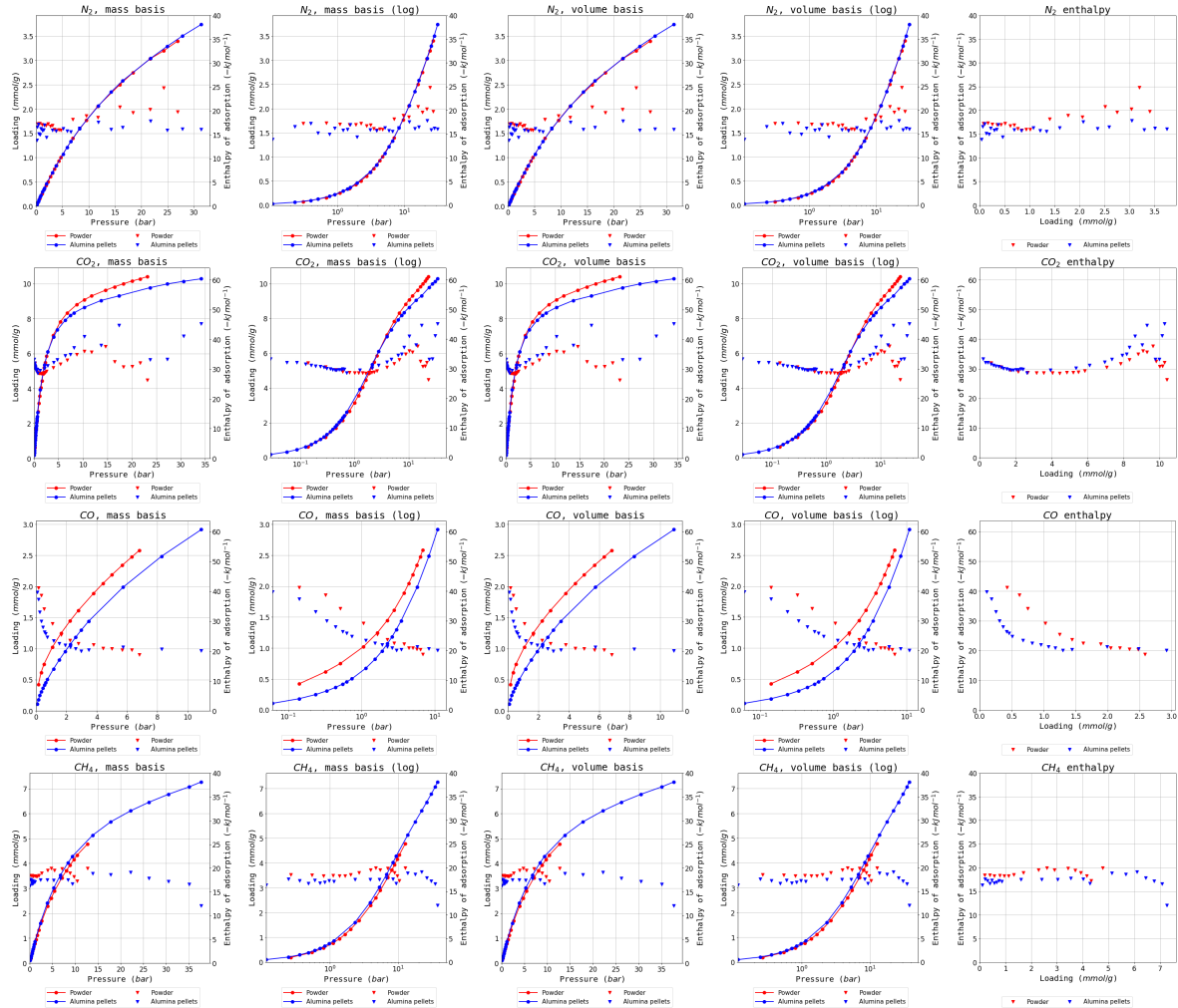


Figure C.3.: Complete isotherm and enthalpy dataset for MIL-127(Fe)

### C. Complete adsorption dataset for shaping study

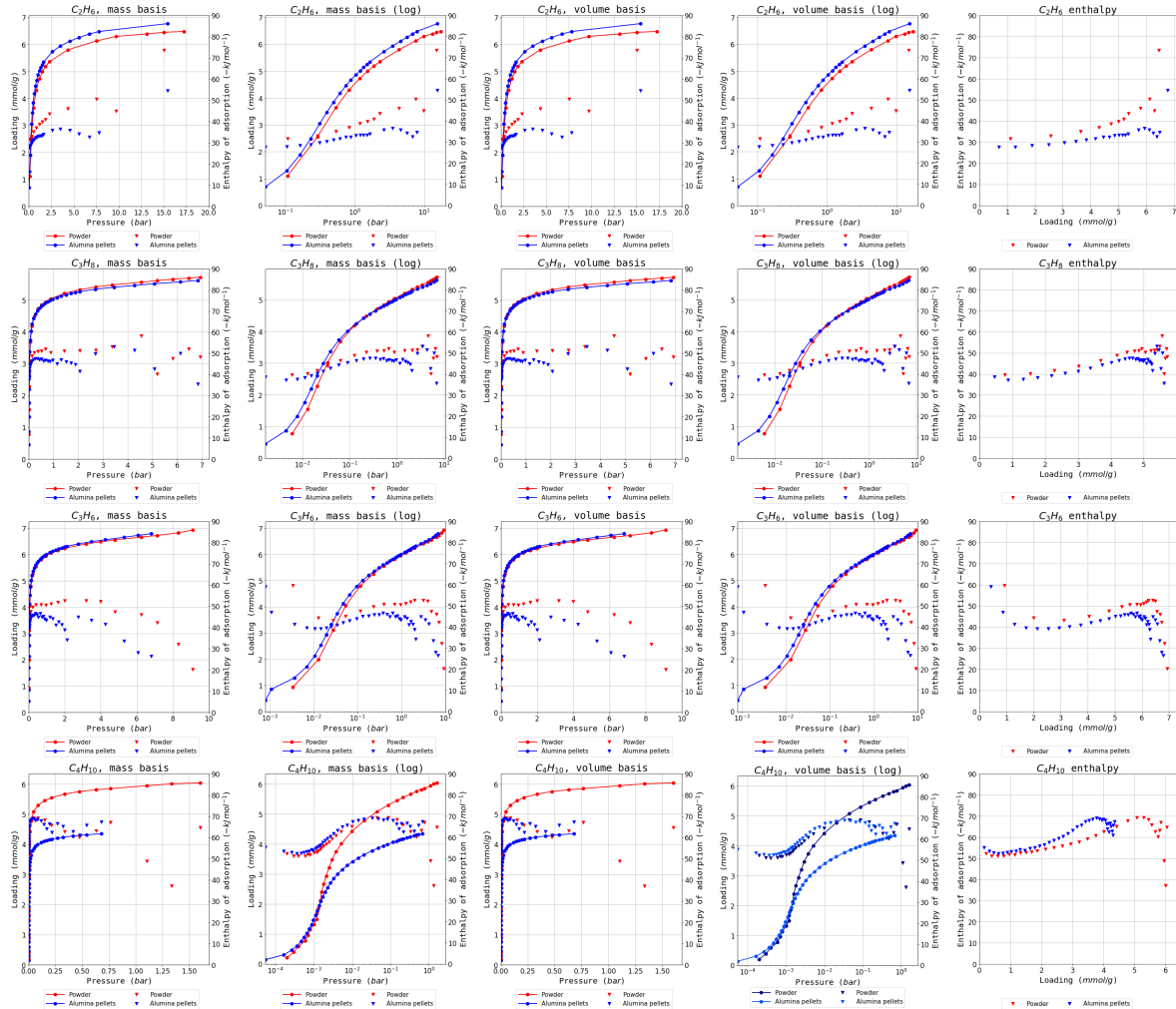


Figure C.3.: Complete isotherm and enthalpy dataset for MIL-127(Fe)